HHS Public Access

Author manuscript

Cell Rep. Author manuscript; available in PMC 2023 February 15.

Published in final edited form as:

Cell Rep. 2023 January 31; 42(1): 112015. doi:10.1016/j.celrep.2023.112015.

Ligands selectively tune the local and global motions of neurotensin receptor 1 (NTS_1)

Fabian Bumbak[1,8,*], **Miquel Pons**[2], **Asuka Inoue**[3], **Juan Carlos Paniagua**[4], **Fei Yan**[5], **Hongwei Wu**[6], **Scott A. Robson**[1], **Ross A.D. Bathgate**[7], **Daniel J. Scott**[7], **Paul R. Gooley**[5], **Joshua J. Ziarek**[1,9,*]

[1]Department of Molecular and Cellular Biochemistry, Indiana University, Bloomington, IN 47405, USA

[2]Department of Inorganic and Organic Chemistry, Universitat de Barcelona, 08028 Barcelona, Spain

[3]Graduate School of Pharmaceutical Sciences, Tohoku University, Sendai, Miyagi 980-8578, Japan

[4]Department of Materials Science and Physical Chemistry & Institute of Theoretical and Computational Chemistry, Universitat de Barcelona, 08028 Barcelona, Spain

[5]Department of Biochemistry and Pharmacology, Bio21 Molecular Science and Biotechnology Institute, University of Melbourne, Parkville, VIC 3010, Australia

[6]Department of Chemistry, Indiana University, Bloomington, IN 47405, USA

[7]The Florey Institute of Neuroscience and Mental Health and Department of Biochemistry and Pharmacology, The University of Melbourne, Parkville, VIC 3010, Australia

[8]Present address: ARC Centre for Cryo-electron Microscopy of Membrane Proteins and Drug Discovery Biology, Monash Institute of Pharmaceutical Sciences, Monash University, Parkville, VIC 3052, Australia

[9]Lead contact

SUMMARY

Nuclear magnetic resonance (NMR) studies have revealed that fast methyl sidechain dynamics can report on entropically-driven allostery. Yet, NMR applications have been largely limited to

*Correspondence: fabian.bumbak@monash.edu (F.B.), jjziarek@indiana.edu (J.J.Z.).

AUTHOR CONTRIBUTIONS

F.B., M.P., A.I., R.A.D.B., D.J.S., P.R.G., and J.J.Z. designed experiments; F.B. and F.Y. prepared NMR samples; F.B., M.P., A.I., J.C.P., and J.J.Z. performed experiments and analyzed data; F.B. and J.J.Z. wrote the manuscript; and all authors reviewed and edited the manuscript.

DECLARATION OF INTERESTS

The authors declare no competing financial interests.

SUPPLEMENTAL INFORMATION

Supplemental information can be found online at https://doi.org/10.1016/j.celrep.2023.112015.

INCLUSION AND DIVERSITY

We support inclusive, diverse, and equitable conduct of research.

the super-microsecond motional regimes of G protein-coupled receptors (GPCRs). We use $^{13}C^{\varepsilon}$-methionine chemical shift-based global order parameters to test if ligands affect the fast dynamics of a thermostabilized GPCR, neurotensin receptor 1 (NTS_1). We establish that the NTS_1 solution ensemble includes substates with lifetimes on several, discrete timescales. The longest-lived states reflect those captured in agonist- and inverse agonist-bound crystal structures, separated by large energy barriers. We observe that the rapid fluctuations of individual methionine residues, superimposed on these long-lived states, respond collectively with the degree of fast, global dynamics correlating with ligand pharmacology. This approach lends confidence to interpreting spectra in terms of local structure and methyl dihedral angle geometry. The results suggest a role for submicrosecond dynamics and conformational entropy in GPCR ligand discrimination.

Graphical Abstract

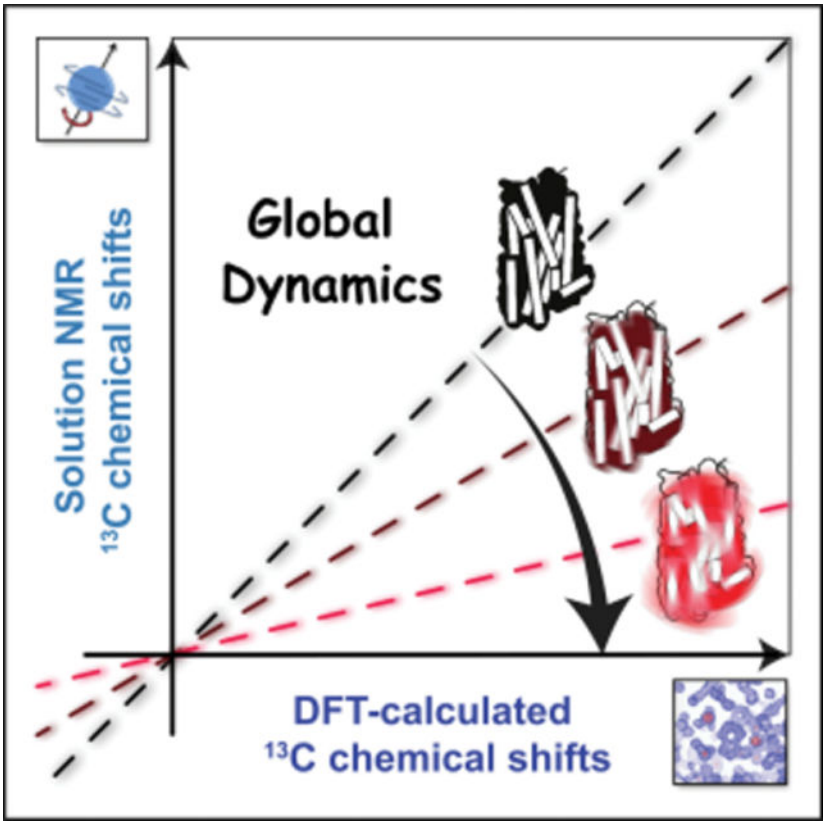

In brief

The very fast motions of proteins can dictate function but are largely invisible to static structural techniques. NMR spectroscopy can observe these motions, but technical challenges have limited their characterization for GPCR activation. Bumbak et al. combine available crystallography data, quantum calculations, and NMR to probe the fast global dynamics of receptors.

INTRODUCTION

G protein-coupled receptors (GPCRs) are the largest family of membrane proteins—comprising approximately 3% of the human genome. They recognize a diverse set of stimuli at the plasma membrane to regulate processes from vision, smell, and taste to immune, neurologic, and reproductive functions. As fundamental components of all major systems, it is no surprise that GPCRs dominate the therapeutic market—accounting for more than 30% of FDA-approved drugs.[1,2] Activation is initiated by agonist binding on the extracellular face, which produces a conformational change on the intracellular side. Unlike many signaling proteins that function as binary switches between “on and off” states, GPCRs feature a ligand-independent basal activity that is increased or decreased upon ligand binding and then further regulated by allosteric modulators. Activated receptors signal intracellularly through G protein and arrestin transducers equally (balanced signaling) or selectively (biased signaling). A single receptor may specifically recognize several ligands and respond uniquely to each, creating a complex conformational landscape. Thus, there is immense therapeutic potential in the ability to tune receptor signaling using partial agonists, biased agonists, and allosteric modulators that is only beginning to be tapped.[3,4]

The principles of allostery, whereby ligand association at one site elicits altered activity at a remote location, have been critical to our understanding of GPCR signaling.[5–8] A dramatic example from crystallography is that orthosteric ligand binding translates the intracellular portions of transmembrane (TM) helices 5 and 6, which are located >40 Å away, outward to accommodate heterotrimeric G proteins.[9] The Monod-Wyman-Changeux (MWC) model of allostery (i.e., conformational selection) posits the preexistence of both inactive and active conformations whose relative populations are modulated by the ligand.[10] Indeed, elegant ^{19}F-nuclear magnetic resonance (NMR) spectroscopy studies confirm these TMs exist as a conformational ensemble that, in most instances, includes more than two stable, low-energy states.[11] Yet, in many instances, the MWC model is unsatisfactory for understanding the full pharmacological landscape of partial agonists, allosteric modulators, and biased agonists.[7,8,11] There is a growing body of evidence that allostery does not necessarily require conformational changes on a scale that can be observed by static structural techniques such as cryoelectron microscopy (cryo-EM) and X-ray crystallography. First theorized by Cooper and Dryden nearly 35 years ago,[12] dynamically driven (DD) allostery asserts that the frequency and amplitude of sub-ns motions around the average conformation (i.e., conformational entropy) can effectively reduce the activation energy barrier between inactive and active modes without the need for structural change.

NMR spectroscopy is uniquely sensitive to dynamical motions across timescales ranging from ps to as long as the molecule is stable.[13] Quantification of fast (ps-ns) backbone amide and side-chain motions, in the form of NMR generalized order parameters, have been used to estimate conformational entropy.[14–19] While the correlation between NMR relaxation rates and conformational entropy is promising, these generalized order parameters are only sensitive to motions faster than the protein’s global rotational correlation time (typically tens of ns for biomolecules in aqueous solution).[20] While recent all-atom molecular dynamics simulations suggest that backbone entropy is correctly captured in the NH generalized order parameter, the slow (super-rotational correlation time) motions of side-chain methyl groups

(inaccessible to NMR relaxation rates) contribute significantly to side-chain conformational entropy.[21]

The high mobility of methionine side-chain methyl groups, compared with branched-chain methyl-containing residues, were generally assumed to provide little information on the overall protein side-chain dynamics and conformational entropy. Yet, the low primary sequence abundance of methionine residues, combined with its relative enrichment in functionally important regions, has made selective methionine labeling one of the most commonly applied approaches to studying GPCRs by NMR.[11] It was recently demonstrated, using density functional theory (DFT) quantum calculations from (static) reference high-resolution X-ray models, that the average methionine methyl ^{13}C chemical shift provides an alternative global order parameter that is sensitive to a much wider range of timescales than relaxation rates.[22] This method relies on the observations (1) that the (de-)shielding effect of neighboring atoms on the methionine methyl chemical shift is comparable, or greater, than the one arising from local side-chain geometry and (2) that experimentally observed chemical shifts are scaled, with respect to those calculated from a static model, by the extent of conformational space sampled by the methionine side chains and neighboring residues. In other words, the experimental chemical shifts are scaled from the rigid-structure calculated values toward those expected from a totally flexible environment. For a given protein, distant methionine side chains experience the same protein-specific scaling and thus sense any large-scale global breathing motion. As a result, a linear correlation is observed between the theoretical and experimental ^{13}C chemical shift values of methionines located far apart in the structure. The (common) degree of local conformational averaging is protein dependent and can be extracted from the slope of the regression line. Thus, this slope can be interpreted as an order parameter for the global flexibility of the protein, as detected locally by multiple methionine side chains in distant parts of the structure. This methionine chemical shift global order parameter (S_{MCS}) can theoretically range from one (completely rigid) to zero (completely averaged).

Here, we focus on a prototypical peptide-binding receptor, neurotensin receptor 1 (NTS_1), to test if S_{MCS} can sense ligand-dependent changes in global receptor dynamics. We functionally validated and assigned the $^{13}C^{\varepsilon}H_3$-methionine resonances of a minimal-methionine NTS_1 variant in the presence of several orthosteric and allosteric ligands. We then compared the experimental $^{13}C^{\varepsilon}$ chemical shifts with DFT-calculated chemical shifts from high-resolution apo, agonist, and inverse agonist-bound NTS_1 crystal structures.[23] Whereas the basal ensemble of the apo receptor appears highly dynamic, agonist and inverse agonist binding tune global motions that differentially modulate receptor rigidity. The linear correlation between experimental chemical shifts and DFT calculations suggested that mechanistic hypotheses could be derived from detailed structural examination. Given the number of $^{13}C^{\varepsilon}H_3$-methionine NMR studies[11] and corresponding high-resolution GPCR crystal structures, our results reveal a tractable approach to exploring global receptor dynamics at timescales longer than the rotational correlation times and length scales encompassing the large distances typically associated with allosteric processes.

RESULTS

NTS_1 construct design and $^{13}C^{e}H_3$-methionine chemical shift assignment

Our study focuses on a selectively $^{13}C^{e}H_3$-methionine-labeled NTS_1 construct, termed $enNTS_1\Delta M4$, which was derived from a previously thermostabilized rat NTS1 ($rNTS_1$) variant ($enNTS_1$)[24] by removing four (M181L, M267L, M293L, and M408V) of the ten endogenous methionine residues (Figure 1A). The sequential differences between $enNTS_1\Delta M4$ and $rNTS_1$ are listed in Table S1. Preliminary experiments showed that mutagenesis did not adversely affect structural integrity as it had little to no observable effect on the remaining resonances' chemical shifts (Figure S1). $M267^{5.68}$, $M293^{ICL3}$, and $M408^{H8}$ (superscript refers to Ballesteros-Weinstein numbering[25]) are solvent exposed and highly degenerate in 2D ^{1}H-^{13}C heteronuclear multiple quantum correlation (HMQC) spectra, while $M181^{ICL2}$ overlaps with $M352^{7.36}$ in some instances. Thus, the mutations simplify the analysis of 2D ^{1}H-^{13}C HMQC spectra (Figure S1) while preserving the structure of $enNTS_1$. $enNTS_1\Delta M4$ retains six endogenous methionine residues ($M204^{4.60}$, $M208^{4.64}$, $M244^{5.45}$, $M250^{5.51}$, $M330^{6.57}$, and $M352^{7.36}$) (Figure 1A) with all, except $M244^{5.45}$, being retained across species. Four of these methionines ($M204^{4.60}$, $M208^{4.64}$, $M330^{6.57}$, and $M352^{7.36}$) are also conserved in all NTS_2 sequences, but $M250^{5.51}$ is the only probe significantly conserved among peptide GPCRs (19%, ranking 2nd after leucine; determined using the GMoS Web Interface, http://lmuc.uab.cat/gmos/).[26]

The functional integrity of $enNTS_1\Delta M4$ was assessed using a cell-based alkaline phosphatase (AP) reporter assay for G protein activation. Stimulation of $G\alpha_q$ and $G\alpha_{12/13}$ leads to ectodomain shedding of an AP-fused transforming growth factor-α (TGF-α), which is then quantified using a colorimetric reporter.[27,29] HEK293A cells were transfected with AP-TGF-α and a NTS_1 plasmid construct. NT8-13, the smallest fully functional fragment corresponding to residues 8–13 of NT,[30] stimulates robust, concentration-dependent G protein coupling to $enNTS_1\Delta M4$ in the TGF-α shedding assay (Figures 1B and S2A). β-Arrestin-1 (βArr1) recruitment was measured using a NanoBiT enzyme complementation system.[31] The large and small fragments of the split luciferase were fused to the N terminus of βArr1 and the C termini of NTS_1 variants, respectively, and these constructs were expressed in HEK293A cells. As a negative control, we used the vasopressin V2 receptor (V2R) C-terminally fused with the small luciferase fragment. The basal βArr1 recruitment of $enNTS_1\Delta M4$ did not increase upon agonist addition (Figures 1C and S2B). $enNTS_1\Delta M4$, $rNTS_1$, and human NTS_1 ($hNTS_1$) were similarly expressed on the cell surface (Figure S2C).

$enNTS_1\Delta M4$ resonances were assigned using a "knockin" strategy starting with the binding-competent, minimal methio nine $enNTS_1\Delta M8$ mutant containing only $M330^{6.57}$ and $M352^{7.36}$. For this approach, six plasmids were engineered with sequentially reintroduced methionine residues. All $enNTS_1$ variants were expressed in *Escherichia coli* by inhibiting the methionine biosynthesis pathway while supplementing a defined medium with $^{13}C^{e}H_3$-methionine. Final NMR samples were prepared in n-dodecyl-β-D-maltopyranoside (DDM) at purities ≥95% using a three-step process.[24] ^{1}H-^{13}C HMQC spectra were collected for each construct in the apo and NT8-13 (agonist)-, SR142948A (inverse agonist)-, and ML314

(βArr-BAM)-bound states; each newly observable resonance was then assigned to the respective residue (Figures 2A and S3–S6).

Ligands modulate local methionine side-chain dynamics

All NMR spectra were collected with identical acquisition parameters at 65 μM [$^{13}C^{\varepsilon}H_3$-methionine]-enNTS$_1$ΔM4; thus, both methionine methyl chemical shift values and signal intensities can be directly compared to monitor the effect of ligands. Intensity decreases are usually caused by line broadening and may reflect changes in the transverse relaxation rate (R_2) and/or exchange broadening. R_2 relaxation results from physical properties of the methyl group on the ps-ns timescale, while exchange broadening reflects conformational interconversion (i.e., the methyl group sensing different chemical environments) in the μs-ms timescale. Throughout the subsequent results subsections, empirically observed changes in intensity (Figure S7) are either analyzed individually between two situations (e.g., ligand free and ligand bound) or pairwise by observing how intensities of two methionine signals respond to multiple changes in their chemical environments (e.g., apo and multiple ligands). For example, signal intensities for both M244$^{5.45}$ and M250$^{5.51}$ decrease (19% and 32%, respectively) upon addition of NT8-13, suggesting that the agonist induces μs-ms motions near the P$^{5.50}$/I$^{3.40}$/F$^{6.44}$ (PIF) motif (Figure S7). In contrast, SR142948A leaves the M250$^{5.51}$ intensity unchanged from the apo state while the peak intensities of M244$^{5.45}$ and M330$^{6.57}$ increase by 14% and 45%, respectively, which may reflect a reduction of basal motions (Figure S7).

Ligands tune global receptor flexibility

The numerous high-resolution NTS$_1$ crystal structures available uniquely positioned us to interpret ligand-dependent methionine methyl carbon chemical shift values in terms of the S_{MCS} global order parameter. We focused our analyses on crystal structures of NTSR1-H4$_X$, an evolved rNTS$_1$ construct with 98% sequence identity to enNTS$_1$ΔM4 across structured regions, in the apo (PBD: 6Z66), NT8-13-bound (PDB: 6YVR), and SR142948A-bound (PDB: 6Z4Q) forms.[23] All enNTS$_1$ΔM4 methionine methyl groups are present in the crystallographic models, except for M352$^{7.36}$ in the SR142948A-bound structure (PDB: 6Z4Q). We confirmed that each structure was of sufficient refinement quality, specifically, possessing methionine S–C bond lengths between 1.77 and 1.80 Å.[22] The eight residue substitutions unique to NTSR1-H4$_X$ are all located beyond the 6 Å spheres around methionine methyl carbons included in the DFT chemical shifts calculations and are unlikely to substantially contribute to the calculated chemical shift values.

Nearly all enNTS$_1$ΔM4 NMR spectra contain multiple resonances assigned to a single methionine where the intensity of each resonance reflects its relative population at thermodynamic equilibrium (Figure 2A). The most intense peaks (i.e., the most populated) show the best correlation with the DFT-calculated chemical shifts, confirming that the lowest energy conformers of the solution ensemble are frequently captured by X-ray structures (Figure 2B). The weaker alternative peaks reflect other well-populated conformations that are exchanging with the crystallographic conformer on the ms-s timescale (Figure 2B). Apo enNTS$_1$ΔM4 possesses narrow, near random-coil chemical shift dispersion that produces a very low S_{MCS} of 0.11; this indicates a very flexible structure in which many other

conformational states, beyond the one captured in the crystal structure, are present in solution. Addition of both orthosteric ligands dramatically increases the S_{MCS}, indicating a substantial contraction of the receptor's structural landscape (Figure 2B). The bulky SR142948A inverse agonist yields the most rigid enNTS$_1$ΔM4 solution structure with an S_{MCS} of 0.47 when M250$^{5.51}$ is excluded due to its weak electron density and unusual orientation (Figure 2B); if the predicted M250$^{5.51}$ chemical shift is instead taken as the average of NT8-13 and apo structures, a similar S_{MCS} of 0.48 is obtained (Figure 2B). The NT8-13 full agonist produced slopes of 0.33 and 0.32 when fitted individually against the DFT-calculated chemical shift values from crystallographic chains A and B, respectively, which is comparable to the ligand-binding domain of the glucocorticoid receptor.[22] The linear correlations between experimental and theoretical chemical shift values confirms (1) that the low-energy crystal structure conformation is largely populated in the solution ensemble and (2) that the methionines, some of which are located 20–30 Å apart, sense common, collective motions across the receptor (Figure 2B). This provides confidence for interpreting the structural origin of $^{13}C^{\varepsilon}H_3$-methionine chemical shifts from the published crystal structures.

Methionine probes of the orthosteric pocket inform on ligand association

Methionines 204$^{4.60}$ and 208$^{4.64}$ are located within the orthosteric pocket and are expected to be sensitive local probes for ligand binding (Figure 3D). In the apo state, M204$^{4.60}$ resonates in the same spectral region where the solvent-exposed methyl groups of M267$^{5.68}$, M293^{ICL3}, and M408^{H8} were observed prior to their removal (Figures 2A and S1). Inspection of the apo-state crystal structure clearly shows M204$^{4.60}$ pointing into the empty binding pocket (Figure S8A). In the absence of direct interactions with other residues, the chemical shifts can be interpreted as indicating that apo-M204$^{4.60}$ is in ~40% χ^3 *trans* conformation,[32] although it is generally recognized that the high flexibility of methionine methyl groups[33] and low energy barriers between rotamers[32] leaves structural interpretation of their ^{13}C chemical shift values quite speculative. Regardless, the NMR chemical shifts, together with the strong resonance intensity (Figures 3A and S7) and the low global order parameter (Figure 2B), indicate that apo-M204$^{4.60}$ is highly mobile. Addition of NT8-13 or SR142948A induces sizeable upfield chemical shift perturbations (Figure 3A). The positions of the M204$^{4.60}$ peak in the apo and NT8-13- and SR142948A-bound forms are approximately aligned along a linear trajectory despite the different nature of the ligands. Thus, it suggests the main effect of the ligands on M204$^{4.60}$ chemical shifts is through the modulation of the contacts with other receptor residues rather than the direct effect of the ligand on the methionine methyl group.

M204$^{4.60}$ lies adjacent to a hydrogen-bond network (E150$^{3.33}$, T153$^{3.36}$, Y154$^{3.37}$, N241$^{5.42}$, T242$^{5.43}$, and R328$^{6.55}$) that couples the orthosteric pocket to the connector region.[23] Whereas the apo-state structure maintains a fully intact network involving all six amino acids (Figure S8A), binding of NT8-13 releases the E150$^{3.33}$–T153$^{3.36}$ and R328$^{6.55}$–T242$^{5.43}$ hydrogen bonds, leading to the formation of N241$^{5.42}$-T153$^{3.36}$ and N241$^{5.42}$–R328$^{6.55}$ interactions as well as an E150$^{3.33}$–R328$^{6.55}$ salt bridge (Figures 3E and S8B). This reorganization positions the R328$^{6.55}$ guanidinium group near the M204$^{4.60}$ methyl (M204$^{4.60}C^{\varepsilon}$–R328$^{6.55}N^{\eta 2}$ distance of 3.8 Å), which may explain the upfield chemical

shift change in the ^{13}C dimension.[22] The upfield ^{1}H chemical shift change may reflect the proximity of E150$^{3.33}O^{\varepsilon 1}$ (4.1 versus 5.2 Å in apo state) as the distances and orientations of the other putative shielding residues, M208$^{4.64}$ and Y146$^{3.29}$, are nearly identical in the two structures. In the NT8-13-bound spectrum, M204$^{4.60}$ appears as three closely clustered peaks, which qualitatively reflects conformational exchange on the ms-s (i.e., slow) timescale. We hypothesize this results from fluctuations within the hydrogen-bond network induced by motions of the bound NT8-13 ligand[34] and/or remodeling of the connector region.[35] SR142948A largely disrupts the network (Figure S8C), leaving only the N241$^{5.42}O^{\delta 1}$–R328$^{6.55}N^{\varepsilon}$ contact and a newly formed hydrogen bond between R328$^{6.55}N^{\eta 1}$ and O5 of SR142948A. This sharply reduces the M204$^{4.60}C^{\varepsilon}$–R328$^{6.55}N^{\eta 2}$ distance to 3.6 Å, which is consistent with its 0.6 ppm further upfield ^{13}C chemical shift.

M208$^{4.64}$ is the only resonance unobservable under all tested conditions. The M208$^{4.64}$ methyl is stably sandwiched between the Y146$^{3.29}$ and P227^{ECL2} side chains and then forms hydrophobic interactions with either the NT8-13 L13 $C^{\delta}H_3$ group or the adamantane cage of SR142948A (Figures S8D–S8F). DFT calculations of these distinct chemical environments predict relative chemical shift values of −0.3, 0.29, and 0.84 ppm, respectively, from the NT8-13, apo, and SR142948A crystal structures. High ms to low ms exchange kinetics between these extreme chemical shifts would be expected to result in substantial exchange broadening; however, it is also possible the signal is overlapped with DDM detergent resonances.

The periphery of the orthosteric pocket undergoes slow timescale dynamics

M330$^{6.57}$, positioned at the periphery of the orthosteric binding site between TM6 and TM7 (Figure 3), shows a complex response to the addition of the various ligands (Figure 3B). In the apo state, M330$^{6.57}$ manifests as a single, downfield resonance whose ^{1}H chemical shift likely reflects subtle de-shielding from the F346$^{7.30}$ and F350$^{7.34}$ aromatic rings,[36] although at 5.3 and 5.5 Å, respectively, their effect on the ^{13}C chemical shift is minimal.[22] The apo-M330$^{6.57}$ carbon chemical shift reflects a near-equivalent 40:60 gauche:*trans* conformational equilibrium in the absence of significant neighbor-induced shielding effects.[32] NT8-13 perturbs M330$^{6.57}$ 0.03 ppm downfield in the ^{1}H dimension and 0.4 ppm upfield in the ^{13}C dimension (Figure 3B). This may reflect contraction of the orthosteric pocket and a concerted twisting of the M330$^{6.57}$-bearing extracellular tip of TM6 that reduces M330$^{6.57}C^{\varepsilon}$–F346$^{7.30}C^{\varepsilon 2}$, M330$^{6.57}C^{\varepsilon}$–F350$^{7.34}C^{\varepsilon 2/\delta 2}$, and M330$^{6.57}C^{\varepsilon}$–Y347$^{7.31}C^{\delta 1}$ distances to 4.2, 3.5, and 5.5 Å, respectively (Figures S8G and S8H). SR142948A moves the M330$^{6.57}$ ^{1}H frequency 0.1 ppm in the opposite direction (Figure 3B), consistent with the extracellular tips of TM6 and TM7 moving outward to accommodate the bulky ligand (Figure 3F). Expansion of the orthosteric pocket increases the M330$^{6.57}C^{\varepsilon}$–F346$^{7.30}C^{\varepsilon 2}$ separation to 5.8 Å, while the F350$^{7.34}$ side chain re-orients to shield the M330$^{6.57}$ methyl. This is accompanied by splitting of the resonance (Figure 2B) into at least three states qualitatively exchanging on the ms-s (i.e., slow) timescale. Van der Waals interactions with the dimethoxyphenyl group of SR148948A may further contribute to the complex behavior seen for M330$^{6.57}$ (Figure S8I).

M352$^{7.36}$ is situated at the extracellular tip of TM7 facing TM1 (Figure 3D) and is unobservable in the apo state (Figure 3C). In the NT8-13-bound state, M352$^{7.36}$ gives three peaks in slow exchange with intensities indicative of their relative population at thermodynamic equilibrium: states A (73.8%), B (13.9%), and C (12.3%). State B is the only observable resonance in the presence of SR142948A but with an absolute intensity 82% lower than with NT8-13 (Figures 3C and S7). NTS_1 crystal structures reveal a substantial ligand-dependent rearrangement of the M352$^{7.36}$ environment (Figures 3G and S8J–S8L). In the apo structure, the M352$^{7.36}C^{\varepsilon}$ points toward the orthosteric binding site between TM7 and TM1 to interact with the aliphatic portion of the K64$^{1.32}$ side chain (3.9 Å), S63$^{1.31}$ (4.0 Å), I129$^{2.66}$ (4.7 Å), V67$^{1.35}$ (4.8 Å), and Y349$^{7.33}$ (5.7 Å). D60$^{1.28}$ plays a central role by engaging the S63$^{1.31}$ hydroxyl and amide as well as the hydroxyl group of Y349$^{7.33}$; this hydrogen-bond network loosely packs the extracellular tips of TM1 and TM7 with the receptor N terminus. The N terminus is largely unresolved apart from N58 and T59, suggesting that it does not stably associate with the orthosteric binding site in the apo state. In the NT8-13-bound structure, the receptor N terminus extends over the orthosteric binding site to contact the ligand, extracellular loop 1 (ECL1), and ECL2. These extensive interactions pack the extracellular tips of TM1 and TM7 tightly around M352$^{7.36}$, fully engaging the loose hydrogen-bond network observed in the apo state (Figures S8J and S8K). In the SR142948A-bound crystal structure, the M352$^{7.36}$ methyl group, all amino acid side chains within a 6 Å radius, the residues responsible for tethering the extracellular portion of TM1 to TM2/7, and the entire receptor N terminus are all unresolved (Figure S8L).[23] Although SR142948A does not directly interact with TM1, this helix undergoes a substantial 3.8–5 Å outward translation as measured from the K64$^{1.32}$ and S63$^{1.33}$ C^{α} positions that expands the pocket and completely dissociates the N terminus.[23]

Taken together, we hypothesize that M352$^{7.36}$ state A reflects the tightly packed TM1/TM2/TM7 interface and engaged receptor N terminus that is only visible in the NT8-13-bound crystal structure, whereas state B represents a dislocated N terminus. State C likely reflects some intermediate combination of states A and B. This is supported by the high correlation between DFT-calculated chemical shifts and those observed for M352$^{7.36}$ state A but not state B (Figure 2B). The absence of M352$^{7.36}$ in the apo-state spectrum likely signifies μs-ms timescale interconversion between an engaged and disengaged N terminus. NT8-13 slows the overall exchange kinetics while stabilizing the engaged N terminus, whereas the inverse agonist SR142948A prefers the disengaged position (Figure 3C).

Methionine probes adjacent to the connector region report on ligand efficacy

The conserved PIF motif, a centrally located hydrophobic triad, connects the orthosteric pocket to the transducer binding site. Structures generally agree that agonist binding pulls the extracellular portion of TM5 inward, which forces I$^{3.40}$ from between P$^{5.50}$/F$^{6.44}$ to permit outward rotation of TM6.[9,35,37,38] As such, $^{13}C^{\varepsilon}H_3$-methionine studies of other class A GPCRs have identified methionine probes on TM5 located below the P$^{5.50}$ kink (M203$^{5.57}$ in α_{1A}AR,[39] M223$^{5.54}$ in β_1AR,[40] and M215$^{5.54}$ in β_2AR[41]) as activation sensors that show efficacy dependent ligand-induced chemical shift changes. The PIF motif in enNTS$_1$ΔM4 consists of P249$^{5.50}$, A157$^{3.40}$, and F317$^{6.44}$ with two methionine probes in TM5, M244$^{5.45}$

and M250$^{5.51}$, located one turn prior to, and immediately following, the kink-inducing P249$^{5.50}$ (Figure 4).

M244$^{5.45}$ shows a clear linear response with NT8-13 inducing upfield ^{1}H (downfield ^{13}C) chemical shift perturbations compared with the apo state, and SR142948A moving M244$^{5.45}$ downfield (upfield ^{13}C; Figure 4A). The simplest explanation for this behavior is a two-state equilibrium (e.g., inactiveactive) in the fast-exchange NMR timescale that is modulated by ligand binding[42]; this is consistent with SR142948A being an inverse agonist[23,43,44] and the hypothesis that efficacy results from the ability of a ligand to stabilize a specific active state.[40,41,45–47] Structural analysis suggests that the M244$^{5.45}$ chemical shift is primarily dominated by its proximity to Y154$^{3.37}$. As mentioned earlier, the Y154$^{3.37}$ side chain is part of a hydrogen-bond network at the bottom of the orthosteric ligand-binding pocket (Figures S8A–S8C). Except for two complexes, the majority of NTS_1 structures suggest that the Y154$^{3.37}$ hydroxyl group hydrogen bonds with orthosteric pocket residues, pulling it away from M244$^{5.45}$, when the receptor is activated (Figure S9). This moves M244$^{5.45}$ toward the shielding F248$^{5.49}$ aromatic ring (Figures 4D and S9B), whereas in the inverse agonist-bound structure, the M244$^{5.45}$ side chain is positioned closer to the edge of the Y154$^{3.37}$ aromatic ring while F248$^{5.49}$ moves out of the 6 Å sphere to produce an overall deshielded environment relative to the apo state (Figures 4E and S9C).

M250$^{5.51}$ is positioned directly adjacent to P249$^{5.50}$ of the PIF motif (Figures 4F, 4G, and S9D–S9F). It populates the most upfield ^{1}H chemical shift of any methyl group observed in our study that, along with the ^{13}C frequency, is relatively invariant regardless of ligand pharmacology (Figure 4B). Its unique resonance frequency is likely dominated by its proximity and orientation to the F317$^{6.44}$ aromatic ring with subtle (de-)shielding contributions from the F246$^{5.47}$ and P249$^{5.50}$ side chains[22] (Figures 4F, 4G, and S9D–S9F). Addition of NT8-13 reduces its peak intensity by 30% relative to apo, which suggests contributions from μs-ms exchange (Figure S7). We calculated that agonist binding induces a 0.034 ppm ^{1}H chemical shift perturbation in M250$^{5.51}$ by subtracting the DFT-calculated chemical shifts of the apo state (PDB: 6Z66) from the agonist-bound state (average of chemical shifts from PDB: 6YVR chains A and B), which is consistent with the experimentally observed 0.030 ppm upfield shift. SR142948A perturbs the ^{1}H chemical shift 0.010 ppm downfield, with respect to the apo-state spectrum, while the peak intensity remains virtually unchanged (Figures 4B and S7). This observed chemical shift is more consistent with DFT calculations using the apo and NT8-13 structures (Figure 2B) than with the 0.301 ppm shift predicted from the NTSR1-H4$_X$:SR142948A complex (Figures 4G and S9F), which implies that the inverse agonist-bound crystal structure does not represent the full conformational repertoire of the NTS_1 PIF motif present in solution.

Methionine chemical shifts provide insight into BAM mechanism

Next, we validated the pharmacology of ML314 using the AP reporter assay for G protein activation and NanoBiT enzyme complementation system for βarr1 recruitment. The βArr-biased allosteric modulator (BAM) ML314 attenuates agonist-mediated G protein activation of enNTS_1ΔM4 in a concentration-dependent manner (Figure S10A) as previously reported[48,49] and has no agonist activity by itself (Figure S10B). Like previous observations

with βArr2, ML314 potentiates NT8-13-mediated βArr1 recruitment (Figure S10C). Although ML314 was previously reported to stimulate βArr1 recruitment independent of NT8-13,[49] we only observe βArr-BAM pharmacology (Figure S10D). It is possible that the agonist pharmacology of ML314 may require even higher ligand concentrations that are incompatible with the NanoBiT assay.

To better understand the underlying mechanisms of ML314's βArr-biased pharmacology,[49] we collected ML314:enNTS$_1$ΔM4 spectra in the presence and absence of NT8-13 (Figures 4 and S11A). Unfortunately, there are no published ML314:NTS$_1$ complex structures to use for DFT calculations. We instead substituted the NT8-13:NTSR1-H4$_X$ crystal (PDB: 6YVR) as a "rigid structure" reference. When using the average of chemical shifts calculated from chain A and chain B, we obtain an S_{MCS} of 0.25 (R^2 = 0.86; Figure S11B). This suggests that the ML314 complex is more flexible than those of the orthosteric ligands but more rigid than the apo receptor. Repeating this procedure with the ML314:NT8-13:enNTS$_1$ΔM4 experimental chemical shifts produced an S_{MCS} of 0.34 (R^2 = 0.95; Figure S11B), which is slightly more rigid than NT8-13:enNTS$_1$ΔM4 (Figure S11C). We can only speculate on ML314's activation mechanisms without a published structure; however, our results may shed light on the binding interface itself. Upon addition of ML314, M330$^{6.57}$ experiences a 0.03 ppm upfield ^{1}H shift and 40% reduction in intensity compared with the apo state (Figures 5B and S7D). Although the chemical shifts of M330$^{6.57}$ in the apo and NT8-13 states are not the same, the peak shape and chemical shift perturbations induced upon the respective addition of ML314 are nearly identical. This consistent chemical shift change could result from a slight repositioning of the four nearby aromatic side chains or as a direct result of ML314 binding.

The ML314 spectrum contains additional minor M330$^{6.57}$ peaks. These signals appear at similar positions as the multiple peaks that are observed with SR142948A (Figures 3B and 5B, green dots). A similar inverse agonist-like effect is manifested in ML314's selection of the M352$^{7.36}$ B resonance (Figure 5C). Upon the co-addition of NT8-13 and ML314, M352$^{7.36}$ state A and B (but not C) peaks are visible with reduced and increased intensities, respectively, compared with NT8-13 alone (Figures S7 and S11A). Crystal structures of receptors bound to pharmacologically related positive allosteric modulators, such as the M2 muscarinic acetylcholine receptor complexed with LY2119620,[50] suggest a mechanism involving closure of the extracellular vestibule similar to transducer-bound conformations. However, SR142948A clearly expands the orthosteric pocket.[23] This leads us to hypothesize that the similarity of SR142948A and ML314 complex spectra instead reflects detachment of the receptor N terminus and local stabilization of extracellular TM1/6/7 (Figures 3C and 5C). ML314 may induce a conformation of the orthosteric binding pocket that allows a more favorable interaction with NT8-13 or even present a secondary NT8-13 binding site.[49]

Conformational changes at M204$^{4.60}$ near the bottom of the orthosteric pocket provide mechanistic hypotheses for BAM pharmacology.[49] ML314 induces upfield shifts of M204$^{4.60}$ in both dimensions and reduces the peak intensity by 54% (Figures S7A and S11A). These chemical shift changes appear along a linear trajectory defined by the apo and NT8-13-bound states. The NT8-13:ML314:enNTS$_1$ΔM4 spectrum closely resembles that of NT8-13 alone (Figure S12), although the split M204$^{4.60}$ peak is reduced to the most

upfield resonance, perhaps mediating BAM-like outcomes, with a 45% reduction in signal intensity (Figure S7A). Three new resonances appear in the vicinity but cannot be assigned to M204$^{4.60}$ based solely on their proximity (Figure S11A).

As the putative allosteric pipeline nears the connector region, resonances appear to exhibit signs of transducer functional selectivity. The M244$^{5.45}$ chemical shifts do not change substantially from the apo state, but ML314 reduces the peak intensity by 24% while giving rise to a nearby second peak (Figures 5D and S7B), again at chemical shifts observed in the presence of SR142948A (Figure 5D, green dot). When both ligands are present, the peak doublet observed in the presence of ML314 is slightly exacerbated with corresponding increases in linewidths (Figure 5D). The ^{1}H chemical shift value is centered halfway between those of either ligand individually; thus, in a sense, ML314 antagonizes the chemical shift perturbation of NT8-13 (Figures 5D and S11A). Nearby M250$^{5.51}$ responds similarly. ML314 has little effect on apo-state chemical shift but reduced the peak intensity by 26% (Figures 5E, S7C, and S11A). Upon addition of both NT8-13 and ML314, the M250$^{5.51}$ ^{1}H chemical shift appears between the peak maxima of individual ligands, while the peak intensity is dramatically reduced >60% (Figures 5E, S7C, and S11A).

DISCUSSION

Chashmniam et al. recently showed that the high intrinsic mobility of methionine methyl groups makes their ^{13}C chemical shift sensitive to global side-chain motions.[22] This observation is particularly powerful as the chemical shift is arguably the most accessible NMR parameter to quantitate. The constant chemical shift scaling of methionine methyl groups situated tens of Å apart suggests that the S_{MCS} is sensitive to long-distance, slow motions that significantly contribute to side-chain conformational entropy but are not detected by methyl relaxation studies.[21]

The experimental $^{13}C^{\varepsilon}H_3$-methionine chemical shifts of enNTS$_1$ΔM4 were compared with those calculated from high-resolution crystal structures (Figures 2B and S11C). The linear correlation for NT8-13 and SR142948A complex chemical shifts establishes that (1) the crystalized conformational states dominate the respective enNTS$_1$ΔM4 solution ensembles, (2) the well-distributed methionine residues are sensitive to collective GPCR motions that are fast on the chemical shift timescale, and (3) ligands selectively tune these dynamics (Figure 6A). The peak duplication, exemplified by M352$^{7.36}$, indicates that the available static structures do not represent the entire conformational ensemble in solution and that there are additional sub-states separated by large energy barriers. SR142948A dramatically reduces enNTS$_1$ΔM4 global flexibility around a conformation incompatible with transducer complexation,[23] whereas the agonist and BAM maintained relatively low global order parameters that are consistent with more frequent excursions to active-like conformers. A similar relationship was recently observed for the isoleucine side-chain dynamics of the A_{2A} adenosine receptor.[51] If we assume that the other major entropic component, (de-)solvation entropy,[52] is not substantially different between orthosteric ligands, it would suggest that inverse agonist binding is more enthalpically driven. This would further indicate that NT8-13 remains relatively mobile upon complexation as previously suggested[34] and as observed for the dynorphin/kappa opioid receptor.[53] It is curious to note that the combined

S_{MCS} of NT8-13 and ML314 is larger than either ligand individually, although it is not additive. We hypothesize this may reflect their underlying pharmacology, where both ligands would be expected to stabilize a sub-set of partially overlapping fluctuations within the conformational ensemble. The narrow dispersion of apo enNTS$_1$ΔM4 ^{13}C chemical shifts was uncorrelated with the crystal structure, suggesting a high degree of conformational averaging. Taken together, our results demonstrate that ligands selectively tune long-range dynamic fluctuations, which suggests a role for DD allostery in receptor activation (Figure 6A).

The correlation between observed and DFT-calculated chemical shifts gave us confidence to interpret ligand-dependent perturbations in terms of their local electronic environment. From this, we can hypothesize on the effects of the yet biophysically uncharacterized ML314 BAM. For example, M352$^{7.36}$ senses a polar network that packs the TM1/7 extracellular tips against the N terminus. Our solution observations agree with recent apo and inverse agonist-bound crystal structures that the N terminus is primarily detached from the orthosteric binding site.[23] While NT8-13 binding indeed stabilizes the NTS$_1$ N terminus with the extracellular vestibule in a lid-like manner, it continues to exchange slowly with a disengaged conformation reflecting previously observed flexibility in the orthosteric pocket (Figure 6B). SR142948A and ML314 both maintain the receptor with a detached N terminus. Yet, ML314 leaves the orthosteric pocket empty while modestly rigidifying fast dynamics, which may provide a mechanism for potentiating NT8-13 efficacy.[48,49] We identify M204$^{4.60}$ of the orthosteric pocket as a sensor for subtle ligand-dependent rearrangements of a polar network that triggers the allosteric communication of extracellular ligand-binding events to the transducer binding site. ML314 alone leads to an observable splitting and hence a reduction of M204$^{4.60}$ exchange rate dynamics and may thus preselect a NT8-13 competent conformation of the orthosteric binding site. M244$^{5.45}$, located one turn above P$^{5.50}$ of the conserved PIF motif (or connector region), exhibits clear efficacy-dependent chemical shift perturbations. While there is no comparable probe from previous ^{13}C$^{\varepsilon}$H$_3$-methionine NMR studies, methionine residues after the P$^{5.50}$ kink typically show strong correlations between chemical shift perturbations and ligand efficacy[39–41,54]; enNTS$_1$ΔM4 M250$^{5.51}$ does for NT8-13 but not SR142948A. While position 5.51 may be too close to the 5.50 hinge to sense the outward rotation of TM5, a similar behavior was observed for M2R M202$^{5.54}$.[55] Perhaps this reflects a general phenomenon in which receptors with shorter side chains at position 3.40, V$^{3.40}$ for M2R and A$^{3.40}$ for NTS$_1$, possess a less tightly packed (i.e., more dynamic) connector region compared with receptors with I$^{3.40}$. Here, we demonstrate an approach for maximizing the information ^{13}C$^{\varepsilon}$H$_3$-methionine probes provide on the thermodynamic, kinetic, and structural aspects of the free-energy landscape.

Limitations of the study

The present study is limited to a thermostabilized receptor solubilized in a DDM detergent micelle. Thermostabilized enNTS$_1$ permits extended data acquisition times that would otherwise be impossible; it binds ligands with similar affinity to rNTS$_1$[56] and couples directly to G protein and βArr,[57] although with reduced affinity (Figures 1 and S2). The DDM detergent micelles minimize line-broadening side effects of slowly tumbling

systems but do not fully recapitulate the physicochemical properties of cellular membranes. We attribute the differential peak intensities to exchange-broadening motions on the intermediate chemical shift timescale (Figure S7), although it is also possible that the peak intensity changes result from ps-ns motions that alter T_1 or intrinsic T_2 relaxation rates.[58] Future experiments will test whether the correlation between concerted receptor motions and the pharmacological efficacy of ligands can be generalized to the GPCR superfamily.

STAR★METHODS

Detailed methods are provided in the online version of this paper and include the following:

RESOURCE AVAILABILITY

Lead contact—Further information and requests for resources and reagents should be directed to and will be fulfilled upon reasonable request by the lead contact, Joshua Ziarek (jjziarek@indiana.edu).

Materials availability—Mutagenic enNTS$_1$ plasmids generated in this study are available from the lead contact under a materials transfer agreement.

Data and code availability

- NMR chemical shift data have been deposited in the Biological Magnetic Resonance Data Bank (BMRB: 51728, 51735, 51736, 51737, and 51738) and are publicly available as of the date of publication.
- This paper does not report original code.
- Any additional information required to reanalyze the data reported in this paper is available from the lead contact upon request.

EXPERIMENTAL MODEL AND SUBJECT DETAILS

This study used the following cell lines: HEK293A (Thermo Fisher Scientific), *E. coli* DH5α (Thermo Fisher Scientific), and *E. coli* OverExpress C43(DE3) (Sigma-Aldrich). All HEK293A cells were grown following the standard protocols. Briefly, they were grown in Dulbecco's Modified Eagle Medium (DMEM 2, Nissui Pharmaceutical) supplemented with 10% fetal bovine serum (Sigma-Aldrich), penicillin (Sigma-Aldrich), streptomycin (Thermo Fisher Scientific), and glutamine (Thermo Fisher Scientific) at 37°C with 5% CO_2. For culturing *E. coli*, general LB media (Thermo Fisher Scientific), ampicillin (Sigma-Aldrich), and IPTG (Goldbio) were used at 37°C at 250 rpm in a shaker incubator.

METHOD DETAILS

enNTS$_1$ constructs and mutagenesis—The previously characterized functional variant enNTS$_1$ (Bumbak et al., 2018) was available in an expression vector (termed pDS170) with an open reading frame encoding an N-terminal maltose-binding protein signal sequence (MBPss), followed by a 10x His tag, a maltose-binding protein (MBP), a NNNNNNNNNNG linker and a HRV 3C protease site (LEVLFQGP) which were linked via a BamHI restriction site (resulting in additional residues GS) to residue T42 of the

receptor. C-terminally T416 of the receptor was linked via a NheI restriction site (resulting in additional residues AS) to an Avi-tag for *in vivo* biotinylation, a HRV 3C protease site, a GGSGGS linker and a monomeric ultra-stable green fluorescent protein (muGFP).[65]

The minimal methionine mutant enNTS$_1$ΔM8 (M330$^{6.57}$/M352$^{7.36}$) was selected[66] from a methionine mutant library obtained by DNA shuffling using the StEP.[67] The DNA shuffling reaction was carried out using PrimeSTAR HS DNA polymerase (Takara, Mountain View, CA), the two primers listed in the STAR Methods section, and pDS170 plasmids carrying the parent templates enNTS$_1$ΔM10 (containing no methionine residues, purchased form GenScript, Piscataway, NJ) and enNTS$_1$ (containing the full set of 10 methionine residues) at a ratio of 5:1. The StEP library was amplified twice using Phusion HF DNA polymerase (NEB, Ipsiwtch, MA) and the two primers listed in the STAR Methods section, separated on agarose gels and extracted using a Bioline Isolate II kit (Bioline, Taunton, MA). The amplified StEP library was then cloned into an expression vector containing a C-terminal mCherry (pDS11-SacB) instead of a muGFP fusion tag and transformed *E. coli* DH5α cells via electroporation at 2500 V using an Eppendorf 2150 electroporator (Eppendorf, Hauppauge, NY) and Biorad GenePulser cuvettes (Biorad, Hercules, CA). Electroporated cells were recovered in SOC medium (2% (w/v) tryptone, 0.5% yeast extract, 0.05% NaCl, 2.5 mM KCl, 10 mM $MgCl_2$, 20 mM glucose, pH 7.0) for 1 h at 37°C prior to further recovery in LB medium (1% (w/v) tryptone, 0.5% (w/v) yeast extract,1% (w/v) NaCl; containing 100 μg/mL ampicillin, 7% (w/v) sucrose, 1% (w/v) glucose) with shaking at 37°C overnight. 15 mL of 2YT medium (1.6% (w/v) tryptone, 1% (w/v) yeast extract, 0.5% (w/v) NaCl; containing 0.2% (w/v) glucose and 100 μg/μL ampicillin) were then inoculated with 7.5×10^8 cells and grown to OD600 = 0.5 at 37°C with shaking. The temperature was then reduced to 20°C and StEP-NTS$_1$ mutant library expression was induced with 250 μM IPTG. Expression was carried-out for approx. 16 h at 20°C with shaking. 12 mL of expression culture corresponding to 1.75×10^{10} cells, were centrifuged at 3000 rpm and 20°C (Thermo Multifuge), washed with 10 mL TKCl (50 mM Tris HCl, pH 7.4, and 150 mM KCl), resuspended in 10 mL TKCl and incubated for 2 h. The TKCl incubated cells were split in 2 × 2 mL; to one tube (sort) 60 nM FAM-NT8-13 (0.86 μL) and to the other tube (competition) 60 nM FAM-NT8-13 (0.86 μL) and 10 μM NT8-13 (20 μL) were added and the mixtures were incubated in the dark for another 1 h at 20°C with shaking. The ligand-incubated cells were then centrifuged at 3000 rpm for 5 min, resuspended in 2 mL (sort) and 400 μL (competition) and filtered into FACS tubes. The cells incubated in the presence of competitor were used to calibrate the background for non-specific binding (FACSAria III, BD Biosciences). From the other tube, 100,000 from the 8–10% most fluorescent cells were directly sorted into 5 mL LB medium containing 1% (w/v) glucose and recovered for 1 h at 37°C and shaking at 225 rpm. After recovery, 250 μL of the library were plated on an LB-agar plate containing 100 μg/mL ampicillin and 1% (w/v) glucose while 100 μg/mL ampicillin and incubated overnight at 37°C. Out of the >2000 colonies 24 were randomly picked and grown in 5 mL LB medium containing 100 μg/mL ampicillin and 1% (w/v) glucose overnight and the DNA was extracted for sequencing. The enNTS$_1$ΔM8 gene was extracted and cloned into the pDS170 expression vector (pDS170-SacB) containing the C-terminal muGFP gene as described above. To test expression and NT8-13 binding pDS170-enNTS$_1$ΔM8 was transformed into DH5α cells and

each grown in 5 mL of 2YT containing 0.2% (w/v) glucose and 100 μg/μL ampicillin to OD600 = 0.5 at 37°C with shaking. The temperature was then reduced to 20°C and gene expression was induced with 250 μM IPTG. Expression was carried-out for approx. 16 h at 20°C with shaking. The next day, 2×10^8 cells were centrifuged at 3000 rpm and 20°C (Thermo Multifuge) and resuspended in 2 × 150 μL TKCl. To one of the aliquots 150 μL of 50 nM 5-TAMRA-NT8-13 in TKCl (sort) and to the other tube 150 μL of 50 nM 5-TAMRA-NT8-13 and 20 μM NT8-13 in TKCl (competition) were added and the mixtures incubated for 2 h at 20°C with shaking. The ligand-incubated cells were then centrifuged at 3000 rpm for 5 min, resuspended in 1 mL TKCl each and analysed using a LSR Fortessa X-20 FACS (BD Bioscience, Franklin Lakes, NJ). The mutant genes enNTS$_1$ΔM7 (M204$^{4.60}$/M330$^{6.57}$/M352$^{7.36}$), enNTS$_1$ΔM6 (M204$^{4.60}$/M208$^{4.64}$/M330$^{6.57}$/M352$^{7.36}$), enNTS$_1$ΔM5 (M204$^{4.60}$/M208$^{4.64}$/M244$^{5.45}$/M330$^{6.57}$/M352$^{7.36}$), enNTS1ΔM4 (M204$^{4.60}$/M208$^{4.64}$/M244$^{5.45}$/M250$^{5.51}$/M330$^{6.57}$/M352$^{7.36}$) and enNTS$_1$ΔM4_M330L (M204$^{4.60}$/M208$^{4.64}$/M244$^{5.45}$/M250$^{5.51}$/M330L/M352$^{7.36}$) were purchased from GenScript (Piscataway, NJ) and subcloned into the expression vector pDS170. All sub-cloning was done using the forward and reverse primers CATCATGGATCCACCTCTGAATCTGACACCGC and CATCATGCTAGCGGTAGAGAACGCGTGGTTAG, respectively and the restriction enzymes BamHI and NheI (NEB, Ipswitch, MA).

Expression and purification of enNTS$_1$ variants— $^{13}C^{\varepsilon}H_3$-methionine labelled enNTS$_1$ variants used for all NMR experiments were expressed as MBP-enNTS$_1$-muGFP fusion protein using the following protocol. 5 mL of a LB day-pre-culture containing 100 mg/L ampicillin and 1% (w/v) glucose were inoculated with a single colony of *E. coli* OverExpress C43(DE3) cells (Sigma-Aldrich) freshly transformed with pDS170-enNTS$_1$. After 9 h (37 °C, 225 rpm) this pre-culture was centrifuged (1700 rcf, at RT, 5 min) and the pellet used to inoculate 250 mL of a defined medium pre-culture and grown overnight (1 L flask, 37 °C, 225 rpm). The defined medium consisted of an autoclaved basal salts solution (30 mM KH_2PO_4, 23 mM K_2HPO_4, 16 mM Na_2HPO_4, 17 mM NaCl, 37 mM NH_4Cl, adjusted to pH 7.4 with NaOH) supplemented with sterile filtered trace metal stock solution (1% v/v),[59] 2 mM $MgSO_4$, 0.4% w/v glucose, 50 mg/L thiamine and 100 mg/L ampicillin. After 13 h the defined medium pre-culture reached an OD600 of approximately 2, was centrifuged and its pellet resuspended into 250 mL of fresh medium of which 10 mL was used to inoculate 500 mL of the same defined medium per 2 L flask. Expression cultures were grown for 6.5 h (37°C, 225 rpm) to an OD600 of 0.4. The flasks were cooled on ice for 2 min at which point 50 mg $^{13}CH_3$-methionine (Cambridge Stable Isotopes) was added along with 100 mg each of lysine, threonine, phenylalanine, and 50 mg each of leucine, isoleucine and valine. The expression cultures were placed into a 16°C incubator for 15 min, then induced with 250 μM isopropyl β-D-1-thiogalactopyranoside (IPTG) and protein expression was carried out at 16°C and 225 rpm for 12–16 h. Expressions were usually carried out in batches of 3 L or 4 L and cell pellets were kept frozen at −80°C until further use.

Purification of enNTS$_1$, enNTS$_1$ΔM1(M208V), enNTS$_1$ΔM7 (M204$^{4.60}$/M330$^{6.57}$/M352$^{7.36}$), enNTS$_1$ΔM8 (M330$^{6.57}$/M352$^{7.36}$), enNTS1ΔM6 (M204$^{4.60}$/M208$^{4.64}$/M330$^{6.57}$/M352$^{7.36}$) and enNTS1ΔM5A (M204$^{4.60}$/M208$^{4.64}$/M244$^{5.45}$/M330$^{6.57}$/M352$^{7.36}$)

was carried out using the following protocol.[56] Cell pellets were thawed on ice, resuspended in 50 mL of 100 mM HEPES, 400 mM NaCl, 20% glycerol, pH 8 with an EDTA free protease inhibitor tablet (Roche), 100 mg lysozyme and 10 mg DNAse. After rocking for 30 min at 4°C the cells were sonicated on ice; mixed with 15 mL of DM solution (1.6 g n-decyl-β-D-maltopyranoside, Anatrace) and 15 mL of CHS/CHAPS solution (0.018 g cholesterol hemi succinate (CHS, Sigma) and 0.09 g CHAPS-hydrate (Sigma)). The solubilization mix was stirred for 2 h at 4°C; centrifuged.

(12,000 rcf, 4°C, 30 min) and the supernatant was filtered using a 45 μm Millex-HV Durapore syringe filter (Merck Millipore), adjusted to 10 mM imidazole and mixed with 3 mL of Talon resin equilibrated in 25 mM.

HEPES, 300 mM NaCl, 10% glycerol, 0.15% DM, pH 8 and rocked for 1.5 h at 4°C. The resin retaining the receptor was washed twice with 25 mL of 25 mM HEPES, 500 mM NaCl, 10% glycerol, 0.15% DM, 10 mM imidazole, 0.2 mM PMSF (phenylmethylsulfonyl fluoride), 8 mM ATP, 10 mM MgCl2, pH 8. Detergent exchange to DDM (n-dodecyl-β-D-maltopyranoside, Anagrade, Anatrace) was initiated by washing the resin twice with 25 mL of 25 mM HEPES, 100 mM NaCl, 10% Glycerol, 0.05% DDM, 0.2 mM PMSF, pH 8. The fusion protein was eluted with 15 mL of 25 mM HEPES, 100 mM NaCl, 10% glycerol, 0.05% DDM, 350 mM imidazole, 0.2 mM PMSF, pH 8. The IMAC eluate was concentrated to 1 mL, exchanged to 25 mM HEPES, 300 mM NaCl, 10% Glycerol, 0.05% DDM, pH 8 using a PD10 desalting column (GE Healthcare). Cleavage of the fusion proteins from the receptor was carried out by adding 100 mM of Na_2SO_4, 1 mM TCEP and 30 μL of GST-tagged HRV 3C protease (96 μM stock produced in house) to the PD10 eluate for 16 h at 4°C. The cleavage mixture was applied to 2 mL of Glutathione Sepharose 4B (GE Healthcare), equilibrated with 20 mL of 25 mM HEPES, 300 mM NaCl, 10% Glycerol, 0.05% DDM, pH 8. Flowthrough and washes (15 mL) were collected, adjusted to 5mM imidazole and applied to 3 mL of Talon resin equilibrated with 50 mL of the same buffer. Flow-through and washes containing cleaved $enNTS_1$ were combined and concentrated to 450 μL. The concentrate was centrifuged (9300 rcf, 4°C, 2 min) and the supernatant loaded onto a Superdex 200 10/300 Increase column (GE Healthcare) equilibrated with 50mM potassium phosphate, 100 mM NaCl, 0.02% DDM, pH 7.4 using an Akta Pure FPLC system (GE Healthcare). SEC was carried out at a flow-rate of 0.5 mL/min. Protein was quantitated using the Amido Black 10B protein assay[68] using bovine serum albumin (BSA) as a standard (0 to 15 μg of 2 mg/mL BSA, Pierce).

The variants $enNTS_1$ΔM4 ($M204^{4.60}$/$M208^{4.64}$/$M244^{5.45}$/$M250^{5.51}$/$M330^{6.57}$/$M352^{7.36}$) and $enNTS_1$ΔM4_M330L ($M204^{4.60}$/$M208^{4.64}$/$M244^{5.45}$/$M250^{5.51}$/M330L/$M352^{7.36}$), were purified using a modified protocol. Elutions from the initial IMAC capture step were directly cleaved with His-tagged HRV 3C protease (produced in-house) prior to concentrating using an Amicon 30 kDa MWCO concentrator (Millipore) and dilution with ion exchange chromatography (IEX) loading buffer (20 mM HEPES pH 8.0, 10% Glycerol, 0.02% DDM) to obtain a combined NaCl/Imidazole/Na_2SO_4 concentration of less than 50 mM. The cleaved receptor solution was then loaded onto a 5 mL HiTrap SP HP column (GE Healthcare) using an Akta Start system (GE Healthcare) and washed with the same buffer until the signal remained stable. The column was then washed with four column volumes of

IEX wash buffer (20 mM HEPES pH 7.4, 10% Glycerol, 63 mM NaCl, 0.02% DDM) after which a 1 mL Ni-NTA HisTrap column (GE Healthcare) was inserted after the HiTrap SP HP column and the system was washed with another 10 mL of IEX wash buffer containing 10 mM Imidazole. The cleaved receptor was the eluted with IEX elution buffer (20 mM HEPES pH 7.4, 10% Glycerol, 1 M NaCl, 0.03% DDM, 20 mM Imidazole) and the receptor containing fractions concentrated to approx. 400 µL for injection onto a S200 Increase SEC column (GE Healthcare) using a 500 µL loop and an Akta Pure System (GE Healthcare). The receptor containing fractions from SEC purification using SEC buffer (50 µM Potassium phosphate pH 7.4, 100 mM NaCl, 0.02% DDM) were then concentrated and buffer exchanged (for NMR experiments) using NMR buffer (50 mM Potassium phosphate pH 7.4, 100 mM NaCl in 100% D_2O) to reduce the residual H_2O concentration to <1%. Protein concentrations were determined using the NanoDrop One system (Thermo Fisher Scientific) and the samples were aliquoted and stored at −80°C until further use. The modified purification protocol comprising the IEX step was found to yield a similar if not higher receptor purity compared to the original protocol containing a reverse IMAC step as judged by SDS-Page. enNTS$_1$ΔM4 used in NMR experiments retains a C-terminal Avi-tag (which was used for capture in ligand-binding and thermostability assays) and the amino acid sequence is:

GPGSTSESDTAGPNSDLDVNTDIYSKVLVTAIYLALFVVGTVGNGVTLFTLARKKSL
QSLQSRVDYYLGSLALSSLLILLFALPVDVYNFIWVHHPWAFGDAGCKGYYFLREAC
TYATALNVVSLSVERYLAICHPFKAKTLLSRSRTKKFISAIWLASALLSLPMLFTMGL
QNLSGDGTHPGGLVCTPIVDTATLRVVIQLNTFMSFLFPMLVASILNTVIARRLTVLVH
QAAEQARVSTVGTHNGLEHSTFNVTIEPGRVQALRRGVLVLRAVVIAFVVCWLPYH
VRRLMFVYISDEQWTTALFDFYHYFYMLSNALVYVSAAINPILYNLVSANFRQVFLS
TLASLSPGWRHRRKKRPTFSRKPNSVSSNHAFSTASGLNDIFEAQKIEWHEGSGLEV
LFQ

NMR spectroscopy—enNTS$_1$ΔM4 and enNTS$_1$ΔM4_M330L NMR spectra were collected on 600 MHz Bruker Avance Neo spectrometers, while enNTS$_1$, enNTS$_1$M208V, enNTS$_1$ΔM8, ΔM7, ΔM6, and ΔM5 spectra (used in Figures S1 and S3–S6) were recorded on a 800 MHz Bruker Avance II spectrometer. All spectrometers were equipped with triple resonance cryoprobes. 2D ^{1}H-^{13}C SOFAST-HMQC spectra[69] were recorded with 25% non-uniform sampling (NUS) at 298 K with a ^{1}H spectral width of 12 ppm (1024 data points in t_2) and a ^{13}C spectral width of 25 ppm (128 data points in t_1), relaxation delays of 400 ms (800 MHz) and 450 ms (600 MHz), and 2048 scans per t1 data point resulting in acquisition times of 8 h (800 MHz) and 10 h (600 MHz) per spectrum. A 2.25 ms PC9 120 degree ^{1}H pulse[70] was applied for excitation and a 1 ms r-SNOB shaped 180 degree ^{1}H pulse[71] was used for refocusing. The ^{13}C carrier frequency was positioned at 17 ppm, and the ^{1}H at 4.7 ppm, while band selective ^{1}H pulses were centered at 2 ppm (800 MHz) and 1.8 ppm (600 MHz). 1D ^{1}H spectra (used for DSS spectral referencing) were recorded at 298 K with a spectral width of 13.7 ppm (2048 data points) and a relaxation delay of 1 s, and 128 scans. Samples measured at 800 MHz were prepared to volumes of 290 µL in 5 mm Shigemi NMR tubes (Shigemi Inc., Allison Park, PA). Samples measured at 600 MHz were prepared to volumes of 160 µL in 3 mm tubes (Willmad). Samples measured at 600 MHz contained 20 µM DSS and 0.05% (w/v) NaN_3. Ligands were added to a final concentration

of 500 μM. NT8-13 (5–10 mM) and SR142948A (20 mM) stock solutions were prepared in 100% D_2O and ML314 (20 mM) in 100% DMSO-d_6. Spectra measured at 600 MHz were referenced against internal DSS and spectra measured at 800 MHz were referenced against D_2O. All 2D ^{1}H-^{13}C SOFAST-HMQC spectra were reconstructed with compressed sensing using qMDD[72] and processed using NMRPipe[61] where data were multiplied by cosinebells and zero-filled once in each dimension. Spectra were analyzed in Sparky (Goddard, T.D. and Kneller, D.G., University of California, San Francisco). All enNTS$_1$ΔM4 spectra in this study are reproduced together in Figure S12.

TGFα shedding assay—HEK293A cells (Thermo Fisher Scientific) were seeded in a 6-well culture plate (Greiner Bio-One) at a concentration of 2×10^5 cells/mL (2 mL per well hereafter) in DMEM (Nissui Pharmaceutical) supplemented with 10% (v/v) FBS (Gibco), glutamine, penicillin, and streptomycin, one day before transfection. The transfection solution was prepared by combining 5 μL of 1 mg/mL polyethylenimine Max solution (Polysciences) and a plasmid mixture consisting of 200 ng ssHA-FLAG-NTS$_1$ and 500 ng alkaline phosphatase (AP)-tagged TGF-α (AP-TGFα; human codon-optimized). One day after incubation, the transfected cells were harvested by trypsinization, neutralized with DMEM containing 10% (v/v) FCS and penicillin–streptomycin, washed once with Hank's Balanced Salt Solution (HBSS) containing 5 mM HEPES (pH 7.4), and resuspended in 6 mL of the HEPES-containing HBSS. The cell suspension was seeded into a 96-well plate at a volume of 80 μL (per well hereafter) and incubated for 30 minutes in a CO_2 incubator. A test ligand (ML314; diluted in 0.01% (w/v) BSA and 5 mM HEPES-containing HBSS (assay buffer) at 10x concentration) or vehicle was added at a volume of 10 μL. After 5 min, a test agonist (NT8-13; serially diluted in assay buffer at 10x concentration) was added and the plate was incubated for 1 h. After centrifugation, conditioned media (80 μL) was transferred to an empty 96-well plate. AP reaction solution (10 mM p-nitrophenylphosphate (*p*-NPP), 120 mM Tris–HCl (pH 9.5), 40 mM NaCl, 10 mM $MgCl_2$) was dispensed into the cell culture plates and plates containing conditioned media (80 μL). Absorbance at 405 nm was measured before and after a 1 h or 2 h incubation at room temperature using a microplate reader (SpectraMax 340 PC384; Molecular Devices). Unless otherwise noted, vehicle-treated AP-TGF-α release signal was set as a baseline. Using Prism 8 software (GraphPad Prism), AP-TGF-α release signals were fitted with a four-parameter sigmoidal concentration-response curve.

NanoBiT-based βArr1 assay—HEK293A cells were seeded in a 6 cm culture dish (Greiner Bio-One) at a concentration of 2×10^5 cells/mL (4 mL per dish) in the FBS-supplemented DMEM. Plasmid transfection was performed by combining 10 μL of the polyethylenimine Max solution and a plasmid mixture consisting of 1 μg ssHA-FLAG-GPCR-SmBiT and 200 ng LgBiT-βArr1 in 400 μL of Opti-MEM. After an incubation for one day, the transfected cells were harvested with 0.5 mM EDTA-containing Dulbecco's PBS (D-PBS), centrifuged, and suspended in 4 mL of HBSS containing 0.01% (w/v) BSA and 5 mM HEPES (pH 7.4) (assay buffer). The cell suspension was dispensed in a white 96-well plate (Greiner Bio-One) at a volume of 70 μL per well and loaded with 20 μL of 50 μM coelenterazine (Carbosynth), diluted in the assay buffer. After 2 h incubation at room temperature, the plate was measured for its baseline luminescence (SpectraMax L,

2PMT model, Molecular Devices). Thereafter, a test ligand (ML314; diluted in assay buffer at 10x concentration) was added at a volume of 10 μL and the plate was incubated for 15 min at room temperature. After a second measurement of luminescence, a test agonist (NT8-13; serially diluted in assay buffer at 6x concentration) were added at a volume of 20 μL and the plate was immediately read as a kinetics mode for 10 min. Luminescence counts recorded from 5 min to 10 min after the agonist addition were averaged and normalized to the initial counts. The fold-change signals were further normalized to the vehicle-treated signal and were plotted as a βArr1 recruitment response. Using the Prism 8 software, the βArr1 recruitment signals were fitted to a four-parameter sigmoidal concentration-response curve.

Flow cytometry analysis—Plasmid transfection into HEK293A cells were performed as described in the TGFα shedding assay section. One-day after transfection, the cells were collected by adding 200 μL of 0.53 mM EDTA-containing D-PBS, followed by 200 μL of 5 mM HEPES (pH 7.4)-containing HBSS. The cell suspension was transferred to a 96-well V-bottom plate in duplicate, blocked with 2% (v/v) goat serum- and 2 mM EDTA-containing D-PBS (blocking buffer; 100 μL per well hereafter) and fluorescently labeled with the anti-FLAG-epitope tag monoclonal antibody (Clone 1E6, FujiFilm Wako Pure Chemicals; 10 μg per ml in the blocking buffer; 25 μL) and a goat anti-mouse IgG secondary antibody conjugated with Alexa Fluor 488 (Thermo Fisher Scientific, 10 μg per mL diluted in the blocking buffer; 25 μL). Live cells were gated with a forward scatter (FS-Peak-Lin) cutoff at the 390 setting, with a gain value of 1.7 and fluorescent signal derived from Alexa Fluor 488 was recorded in the FL1 channel.

DFT chemical shift calculations—DFT calculations of methionine $^{13}C^{\varepsilon}H_3$ chemical shifts were performed using apo (PBD 6Z66), NT8-13-bound (PDB 6YVR), and SR142948A-bound (PDB 6Z4Q) crystal structures as previously detailed.[22] A detailed step by step protocol for non-experts is provided.

The quality of the chemical shift predictions of methionine methyl groups is strongly dependent on the quality of the X-ray model of the methionine side chain. We used the following criteria to choose X-ray structures: a) high resolution structures (2 Å or better) with b) methyl carbon-sulfur distances in the refined model between 1.77 and 1.80 Å. Calculated chemical shifts are strongly dependent on the carbon-sulfur distance. Although this effect can be corrected empirically, large chemical shift deviations are often associated with other inaccuracies in the modelling of the electron density around the methionine side chain and can lead to poor chemical shift predictions.

Truncated models were generated using Chimera[62] by selecting entire residues in the protein with at least one atom at a distance less than 6 Å from the methionine methyl carbon of interest. Those amino acids were selected by clicking on the desired carbon and using the “select zone” option on the “selection” menu with the options “< 6 Å from currently selected atoms” and “select all atoms/bonds of any residue in selection zone”. The selection was saved with the “write pdb” command from the “actions” menu and the option “save selected atom only”. This file was named “NameOfProtein_MetNumber.pdb” and the procedure was

repeated for each of the methionine residues. Avoid using filenames starting with a number, as often happens if the PDB code is used to name the protein.

Each file containing the residues around a methionine was opened with Avogadro 1.2.0[71] and hydrogens were added to the newly generated amino and carbonyl ends of the disconnected peptide bonds to generate neutral amino and aldehyde groups. Use the command “Add hydrogens at pH 10” in the “compile” menu. Two versions of each file were saved with the options “save as pdb” (*.pdb) and “save as Gaussian cartesian input” (*.gau).

The python script “programCheckPDBavogadro.py” was then executed on the pdb file to obtain the numberings of the carbon atom of the terminal methyl group of the methionine and its bounded protons, to be used to automatically extract the chemical shifts from the output file of the Gaussian calculation. This script also identifies potentially charged (Asp, Glu, Lys, Arg, His) and cysteine residues, whose proper degree of protonation must be checked, and calculates the global charge of the ensemble.

The python script “programAddGausOptions.py” was then executed on the *.gau file. This script includes the keywords: #B972/6-31G(d,p) SCF = tight scrf=(iefpcm.solvent = water) NMR. The output of the spript is a file named NameOfProtein_MetNumber_new.gjf.

This file was opened with gaussview and the data produced by “programCheckPDBavogadro.py” was used to check for the correct protonation of individual ionizable groups and the total molecular charge. To add a hydrogen, we used the “Add Valence” command in the Builder menu by clicking on the atom with the missing proton. To remove a proton, the “Delete Atom” command in the Builder menu was selected followed by clicking on the hydrogen atom to be deleted. The total charge can be modified using a text editor, such as TextEdit in MacOS, Notepad in Windows or vi in Unix, by changing the first number that appears in the line just before the list of coordinates so that it reflects the total charge of the ensemble (typically 0, +1, or −1).

The *.gjf file is the input file for the Gaussian-09 program[64] that is usually run on a server through a script that provides the names for the input and output files, the number of processors to be used and the queue parameters. A template script is typically provided by the system manager and can be edited with a text editor.

When the calculation is terminated successfully, an output file (typically*.out) is generated. The isotropic shieldings can be automatically extracted from this file using the python script “programExtrShiftGausOutIndividualFiles.py”.

Isotropic shielding values were similarly calculated for the trimethylsilylpropanesulfonate (DSS) chemical shift reference. Methionine chemical shifts (δ) are calculated form the DSS shielding value (^{13}C: 188.6197 ppm, ^{1}H: 31.52761 ppm) minus the methionine shielding value.

Linear regression was then used to calculate the correlation between experimental (δ_{exp}) and calculated (δ_{calc}) carbon chemical shifts. The methionine chemical shift order parameter

(S_{MCS}) is the slope of the line. The value of the y-intercept (b_i) also follows a trend related to the overall flexibility of the protein. To directly compare the regressions of each ligand state in Figure S11, we eliminated the contribution of the intercept by plotting $\Delta\delta_{corr} = \delta_{exp} - \delta_{calc} - b_i$ versus δ_{calc} where $\Delta\delta_{corr}$ is corrected chemical shift, δ_{exp} is experimental chemical shift, and δ_{calc} is calculated chemical shift. The slope of this line is S_{MCS}^{-1}.

QUANTIFICATION AND STATISTICAL ANALYSIS

All G protein activation and βArr1 recruitment data are presented as mean ± standard error of the mean. Functional data analyses were performed using GraphPad Prism 8 (GraphPad Software). Linear regression of experimental and DFT-calculated chemical shifts was performed using Microsoft Excel (Microsoft).

Supplementary Material

Refer to Web version on PubMed Central for supplementary material.

ACKNOWLEDGMENTS

We would like to thank Dr. Piotr Mroz (Indiana University) for synthesis of NT8-13, Dr. Vanta Jameson and Dr. Josh Kie (The University of Melbourne) for assistance with flow cytometry, and Prof. Andrew L. Lee (The University of North Carolina at Chapel Hill) for fruitful discussions. The 14.1 T spectrometer at Indiana University used in this study was generously supported by the Indiana University Fund. The project was funded by KAKENHI 21H04791 (A.I.) and 21H051130 (A.I.); JPJSBP120213501 (A.I.) from Japan Society for the Promotion of Science (JSPS); LEAP JP20gm0010004 (A.I.); BINDS JP20am0101095 (A.I.) from the Japan Agency for Medical Research and Development (AMED); FOREST JPMJFR215T (A.I.) and JST Moonshot Research and Development Program JPMJMS2023 (A.I.) from Japan Science and Technology Agency (JST); Daiichi Sankyo Foundation of Life Science (A.I.); Takeda Science Foundation (A.I.); Ono Medical Research Foundation (A.I.); Uehara Memorial Foundation (A.I.); Agencia Estatal de Investigación, Spain grant PID2019-104914RB-I00 (J.C.P. and M.P.); Ministerio de Ciencia e Innovación, María de Maseztu grant CEX2021-001202-M (J.C.P. and M.P.); Australian National Health and Medical Research Council (NHMRC) grants 1081844 and 1141034 (R.A.D.B., D.J.S., and P.R.G.); Indiana Precision Health Initiative (J.J.Z.); and National Institutes of Medicine (NIH) grants R00GM115814 (J.J.Z.) and R35GM143054 (J.J.Z.).

REFERENCES

1. Hauser AS, Attwood MM, Rask-Andersen M, Schiöth HB, and Gloriam DE (2017). Trends in GPCR drug discovery: new agents, targets and indications. Nat. Rev. Drug Discov. 16, 829–842. 10.1038/nrd.2017.178. [PubMed: 29075003]
2. Hauser AS, Chavali S, Masuho I, Jahn LJ, Martemyanov KA, Gloriam DE, and Babu MM (2018). Pharmacogenomics of GPCR drug targets. Cell 172, 41–54.e19. 10.1016/j.cell.2017.11.033. [PubMed: 29249361]
3. Administration, U.F.a.D. (2020). Drug Trials Snapshots (OLINVYK).
4. Administration, U.F.a.D. (2020). FDA Approves New Opioid for Intravenous Use in Hospitals, Other Controlled Clinical Settings.
5. Kern D, and Zuiderweg ERP (2003). The role of dynamics in allosteric regulation. Curr. Opin. Struct. Biol. 13, 748–757. 10.1016/j.sbi.2003.10.008. [PubMed: 14675554]
6. Motlagh HN, Wrabl JO, Li J, and Hilser VJ (2014). The ensemble nature of allostery. Nature 508, 331–339. 10.1038/nature13001. [PubMed: 24740064]
7. Thal DM, Glukhova A, Sexton PM, and Christopoulos A (2018). Structural insights into G-protein-coupled receptor allostery. Nature 559, 45–53. 10.1038/s41586-018-0259-z. [PubMed: 29973731]
8. Lane JR, May LT, Parton RG, Sexton PM, and Christopoulos A (2017). A kinetic view of GPCR allostery and biased agonism. Nat. Chem. Biol. 13, 929–937. 10.1038/nchembio.2431. [PubMed: 28820879]

9. Rasmussen SGF, Choi HJ, Fung JJ, Pardon E, Casarosa P, Chae PS, Devree BT, Rosenbaum DM, Thian FS, Kobilka TS, et al. (2011). Structure of a nanobody-stabilized active state of the beta(2) adrenoceptor. Nature 469, 175–180. 10.1038/nature09648. [PubMed: 21228869]
10. Monod J, Wyman J, and Changeux JP (1965). On the nature of allosteric transitions: a plausible model. J. Mol. Biol. 12, 88–118. [PubMed: 14343300]
11. Shimada I, Ueda T, Kofuku Y, Eddy MT, and Wüthrich K (2019). GPCR drug discovery: integrating solution NMR data with crystal and cryo-EM structures. Nat. Rev. Drug Discov. 18, 59–82. 10.1038/nrd.2018.180. [PubMed: 30410121]
12. Cooper A, and Dryden DT (1984). Allostery without conformational change. A plausible model. Eur. Biophys. J. 11, 103–109. 10.1007/bf00276625. [PubMed: 6544679]
13. Ziarek JJ, Baptista D, and Wagner G (2018). Recent developments in solution nuclear magnetic resonance (NMR)-based molecular biology. J. Mol. Med. (Berl.) 96, 1–8. 10.1007/s00109-017-1560-2. [PubMed: 28643003]
14. Akke M, Brueschweiler R, and Palmer AG (1993). NMR order parameters and free energy: an analytical approach and its application to cooperative calcium(2+) binding by calbindin D9k. J. Am. Chem. Soc. 115, 9832–9833. 10.1021/ja00074a073.
15. Yang D, and Kay LE (1996). Contributions to conformational entropy arising from bond vector fluctuations measured from NMR-derived order parameters: application to protein folding. J. Mol. Biol. 263, 369–382. 10.1006/jmbi.1996.0581. [PubMed: 8913313]
16. Sharp KA, O'Brien E, Kasinath V, and Wand AJ (2015). On the relationship between NMR-derived amide order parameters and protein backbone entropy changes. Proteins 83, 922–930. 10.1002/prot.24789. [PubMed: 25739366]
17. Caro JA, Harpole KW, Kasinath V, Lim J, Granja J, Valentine KG, Sharp KA, and Wand AJ (2017). Entropy in molecular recognition by proteins. Proc. Natl. Acad. Sci. USA 114, 6563–6568. 10.1073/pnas.1621154114. [PubMed: 28584100]
18. Kasinath V, Sharp KA, and Wand AJ (2013). Microscopic insights into the NMR relaxation-based protein conformational entropy meter. J. Am. Chem. Soc. 135, 15092–15100. 10.1021/ja405200u. [PubMed: 24007504]
19. Marlow MS, Dogan J, Frederick KK, Valentine KG, and Wand AJ (2010). The role of conformational entropy in molecular recognition by calmodulin. Nat. Chem. Biol. 6, 352–358. 10.1038/nchembio.347. [PubMed: 20383153]
20. Cavanagh J (2007). Protein NMR Spectroscopy: Principles and Practice, 2nd Edition (Academic Press).
21. Hoffmann F, Mulder FAA, and Schäfer LV (2022). How much entropy is contained in NMR relaxation parameters? J. Phys. Chem. B 126, 54–68. 10.1021/acs.jpcb.1c07786. [PubMed: 34936366]
22. Chashmniam S, Teixeira JMC, Paniagua JC, and Pons M (2021). A methionine chemical shift based order parameter characterizing global protein dynamics. Chembiochem 22, 1001–1004. 10.1002/cbic.202000701. [PubMed: 33166021]
23. Deluigi M, Klipp A, Klenk C, Merklinger L, Eberle SA, Morstein L, Heine P, Mittl PRE, Ernst P, Kamenecka TM, et al. (2021). Complexes of the neurotensin receptor 1 with small-molecule ligands reveal structural determinants of full, partial, and inverse agonism. Sci. Adv. 7, eabe5504. 10.1126/sciadv.abe5504. [PubMed: 33571132]
24. Bumbak F, Keen AC, Gunn NJ, Gooley PR, Bathgate RAD, and Scott DJ (2018). Optimization and 13CH3 methionine labeling of a signaling competent neurotensin receptor 1 variant for NMR studies. Biochim. Biophys. Acta Biomembr. 1860, 1372–1383. 10.1016/j.bbamem.2018.03.020. [PubMed: 29596791]
25. Ballesteros JA, and Weinstein H (1995). Integrated methods for the construction of three-dimensional models and computational probing of structure-function relations in G protein-coupled receptors. Methods Neurosci. 25, 366–428. 10.1016/S1043-9471(05)80049-7.
26. Kobilka BK, and Deupi X (2007). Conformational complexity of G-protein-coupled receptors. Trends Pharmacol. Sci. 28, 397–406. 10.1016/j.tips.2007.06.003. [PubMed: 17629961]
27. Inoue A, Ishiguro J, Kitamura H, Arima N, Okutani M, Shuto A, Higashiyama S, Ohwada T, Arai H, Makide K, and Aoki J (2012). TGFα shedding assay: an accurate and versatile method

for detecting GPCR activation. Nat. Methods 9, 1021–1029. 10.1038/nmeth.2172. [PubMed: 22983457]

28. Shihoya W, Izume T, Inoue A, Yamashita K, Kadji FMN, Hirata K, Aoki J, Nishizawa T, and Nureki O (2018). Crystal structures of human ET(B) receptor provide mechanistic insight into receptor activation and partial activation. Nat. Commun. 9, 4711. 10.1038/s41467-018-07094-0. [PubMed: 30413709]
29. Inoue A, Raimondi F, Kadji FMN, Singh G, Kishi T, Uwamizu A, Ono Y, Shinjo Y, Ishida S, Arang N, et al. (2019). Illuminating G-protein-coupling selectivity of GPCRs. Cell 177, 1933–1947.e25. 10.1016/j.cell.2019.04.044. [PubMed: 31160049]
30. Carraway R, and Leeman SE (1975). The amino acid sequence of a hypothalamic peptide, neurotensin. J. Biol. Chem. 250, 1907–1911. 10.1016/S0021-9258(19)41780-8. [PubMed: 1167549]
31. Dixon AS, Schwinn MK, Hall MP, Zimmerman K, Otto P, Lubben TH, Butler BL, Binkowski BF, Machleidt T, Kirkland TA, et al. (2016). NanoLuc complementation reporter optimized for accurate measurement of protein interactions in cells. ACS Chem. Biol. 11, 400–408. 10.1021/acschembio.5b00753. [PubMed: 26569370]
32. Butterfoss GL, DeRose EF, Gabel SA, Perera L, Krahn JM, Mueller GA, Zheng X, and London RE (2010). Conformational dependence of 13C shielding and coupling constants for methionine methyl groups. J. Biomol. NMR 48, 31–47. 10.1007/s10858-010-9436-6. [PubMed: 20734113]
33. Mittermaier A, Kay LE, and Forman-Kay JD (1999). Analysis of deuterium relaxation-derived methyl axis order parameters and correlation with local structure. J. Biomol. NMR 13, 181–185. 10.1023/a:1008387715167. [PubMed: 20700817]
34. Cong X, Fiorucci S, and Golebiowski J (2018). Activation dynamics of the neurotensin G protein-coupled receptor 1. J. Chem. Theor. Comput. 14, 4467–4473. 10.1021/acs.jctc.8b00216.
35. Dror RO, Arlow DH, Maragakis P, Mildorf TJ, Pan AC, Xu H, Borhani DW, and Shaw DE (2011). Activation mechanism of the beta2-adrenergic receptor. Proc. Natl. Acad. Sci. USA 108, 18684–18689. 10.1073/pnas.1110499108. [PubMed: 22031696]
36. Baranac-Stojanović M, Koch A, and Kleinpeter E (2012). Is the conventional interpretation of the anisotropic effects of C=C double bonds and aromatic rings in NMR spectra in terms of the π-electron shielding/deshielding contributions correct? Chemistry 18, 370–376. 10.1002/chem.201101882. [PubMed: 22135110]
37. Hilger D (2021). The role of structural dynamics in GPCR-mediated signaling. FEBS J. 288, 2461–2489. 10.1111/febs.15841. [PubMed: 33871923]
38. Manglik A, Kim TH, Masureel M, Altenbach C, Yang Z, Hilger D, Lerch MT, Kobilka TS, Thian FS, Hubbell WL, et al. (2015). Structural insights into the dynamic process of β2-adrenergic receptor signaling. Cell 161, 1101–1111. 10.1016/j.cell.2015.04.043. [PubMed: 25981665]
39. Wu F-J, Williams LM, Abdul-Ridha A, Gunatilaka A, Vaid TM, Kocan M, Whitehead AR, Griffin MDW, Bathgate RAD, Scott DJ, and Gooley PR (2020). Probing the correlation between ligand efficacy and conformational diversity at the α1A-adrenoreceptor reveals allosteric coupling of its microswitches. J. Biol. Chem. 295, 7404–7417. 10.1074/jbc.RA120.012842. [PubMed: 32303636]
40. Solt AS, Bostock MJ, Shrestha B, Kumar P, Warne T, Tate CG, and Nietlispach D (2017). Insight into partial agonism by observing multiple equilibria for ligand-bound and Gs-mimetic nanobody-bound β1-adrenergic receptor. Nat. Commun. 8, 1795. 10.1038/s41467-017-02008-y. [PubMed: 29176642]
41. Kofuku Y, Ueda T, Okude J, Shiraishi Y, Kondo K, Maeda M, Tsujishita H, and Shimada I (2012). Efficacy of the beta(2)-adrenergic receptor is determined by conformational equilibrium in the transmembrane region. Nat. Commun. 3, 1045. 10.1038/ncomms2046. [PubMed: 22948827]
42. Kleckner IR, and Foster MP (2011). An introduction to NMR-based approaches for measuring protein dynamics. Biochim. Biophys. Acta 1814, 942–968. 10.1016/j.bbapap.2010.10.012. [PubMed: 21059410]
43. Barroso S, Richard F, Nicolas-Ethève D, Kitabgi P, and Labbé-Jullié C (2002). Constitutive activation of the neurotensin receptor 1 by mutation of Phe(358) in Helix seven. Br. J. Pharmacol. 135, 997–1002. 10.1038/sj.bjp.0704546. [PubMed: 11861328]

44. Kling RC, Plomer M, Lang C, Banerjee A, Hübner H, and Gmeiner P (2016). Development of covalent ligand-receptor pairs to study the binding properties of nonpeptidic neurotensin receptor 1 antagonists. ACS Chem. Biol. 11, 869–875. 10.1021/acschembio.5b00965. [PubMed: 26808719]
45. Frei JN, Broadhurst RW, Bostock MJ, Solt A, Jones AJY, Gabriel F, Tandale A, Shrestha B, and Nietlispach D (2020). Conformational plasticity of ligand-bound and ternary GPCR complexes studied by (19)F NMR of the beta1-adrenergic receptor. Nat. Commun. 11, 669. 10.1038/s41467-020-14526-3. [PubMed: 32015348]
46. Isogai S, Deupi X, Opitz C, Heydenreich FM, Tsai CJ, Brueckner F, Schertler GFX, Veprintsev DB, and Grzesiek S (2016). Backbone NMR reveals allosteric signal transduction networks in the beta1-adrenergic receptor. Nature 530, 237–241. 10.1038/nature16577. [PubMed: 26840483]
47. Kofuku Y, Ueda T, Okude J, Shiraishi Y, Kondo K, Mizumura T, Suzuki S, and Shimada I (2014). Functional dynamics of deuterated beta2-adrenergic receptor in lipid bilayers revealed by NMR spectroscopy. Angew. Chem., Int. Ed. Engl. 53, 13376–13379. 10.1002/anie.201406603. [PubMed: 25284766]
48. Barak LS, Bai Y, Peterson S, Evron T, Urs NM, Peddibhotla S, Hedrick MP, Hershberger P, Maloney PR, Chung TDY, et al. (2016). ML314: a biased neurotensin receptor ligand for methamphetamine abuse. ACS Chem. Biol. 11, 1880–1890. 10.1021/acschembio.6b00291. [PubMed: 27119457]
49. Peddibhotla S, Hedrick MP, Hershberger P, Maloney PR, Li Y, Milewski M, Gosalia P, Gray W, Mehta A, Sugarman E, et al. (2013). Discovery of ML314, a brain penetrant nonpeptidic beta-arrestin biased agonist of the neurotensin NTR1 receptor. ACS Med. Chem. Lett. 4, 846–851. 10.1021/Ml400176n. [PubMed: 24611085]
50. Kruse AC, Ring AM, Manglik A, Hu J, Hu K, Eitel K, Hübner H, Pardon E, Valant C, Sexton PM, et al. (2013). Activation and allosteric modulation of a muscarinic acetylcholine receptor. Nature 504, 101–106. 10.1038/nature12735. [PubMed: 24256733]
51. Clark LD, Dikiy I, Chapman K, Rödström KE, Aramini J, LeVine MV, Khelashvili G, Rasmussen SG, Gardner KH, and Rosenbaum DM (2017). Ligand modulation of sidechain dynamics in a wild-type human GPCR. Elife 6, e28505. 10.7554/eLife.28505. [PubMed: 28984574]
52. Leavitt S, and Freire E (2001). Direct measurement of protein binding energetics by isothermal titration calorimetry. Curr. Opin. Struct. Biol. 11, 560–566. 10.1016/s0959-440x(00)00248-7. [PubMed: 11785756]
53. O'Connor C, White KL, Doncescu N, Didenko T, Roth BL, Czaplicki G, Stevens RC, Wüthrich K, and Milon A (2015). NMR structure and dynamics of the agonist dynorphin peptide bound to the human kappa opioid receptor. Proc. Natl. Acad. Sci. USA 112, 11852–11857. 10.1073/pnas.1510117112. [PubMed: 26372966]
54. Okude J, Ueda T, Kofuku Y, Sato M, Nobuyama N, Kondo K, Shiraishi Y, Mizumura T, Onishi K, Natsume M, et al. (2015). Identification of a conformational equilibrium that determines the efficacy and functional selectivity of the μ-opioid receptor. Angew. Chem., Int. Ed. Engl. 54, 15771–15776. 10.1002/anie.201508794. [PubMed: 26568421]
55. Xu J, Hu Y, Kaindl J, Risel P, Hübner H, Maeda S, Niu X, Li H, Gmeiner P, Jin C, and Kobilka BK (2019). Conformational complexity and dynamics in a muscarinic receptor revealed by NMR spectroscopy. Mol. Cell 75, 53–65.e7. 10.1016/j.molcel.2019.04.028. [PubMed: 31103421]
56. Bumbak F, Bathgate RAD, Scott DJ, and Gooley PR (2019). Expression and purification of a functional E. coli 13CH3-methionine-labeled thermostable neurotensin receptor 1 variant for solution NMR studies. In G Protein-Coupled Receptor Signaling: Methods and Protocols, Tiberi M, ed. (Springer New York), pp. 31–55. 10.1007/978-1-4939-9121-1_3.
57. Dixon AD, Inoue A, Robson SA, Culhane KJ, Trinidad JC, Sivaramakrishnan S, Bumbak F, and Ziarek JJ (2022). Effect of ligands and transducers on the neurotensin receptor 1 conformational ensemble. J. Am. Chem. Soc. 144, 10241–10250. 10.1021/jacs.2c00828. [PubMed: 35647863]
58. Luginbühl P, and Wüthrich K (2002). Semi-classical nuclear spin relaxation theory revisited for use with biological macromolecules. Prog. Nucl. Magn. Reson. Spectrosc. 40, 199–247. 10.1016/S0079-6565(01)00043-7.
59. Cai M, Huang Y, Sakaguchi K, Clore GM, Gronenborn AM, and Craigie R (1998). An efficient and cost-effective isotope labeling protocol for proteins expressed in Escherichia coli. J. Biomol. NMR 11, 97–102. 10.1023/a:1008222131470. [PubMed: 9566315]

60. Kazimierczuk K, and Orekhov VY (2011). Accelerated NMR Spectroscopy by Using Compressed Sens-ing. Angew. Chem.-Int. Edit. 50, 5556–5559.

61. Delaglio F, Grzesiek S, Vuister GW, Zhu G, Pfeifer J, and Bax A (1995). NMRPipe: a multidimensional spectral processing system based on UNIX pipes. J. Biomol. NMR 6, 277–293. 10.1007/BF00197809. [PubMed: 8520220]

62. Pettersen EF, Goddard TD, Huang CC, Couch GS, Greenblatt DM, Meng EC, and Ferrin TE (2004). UCSF Chimera–a visualization system for exploratory research and analysis. J. Comput. Chem. 25, 1605–1612. 10.1002/jcc.20084. [PubMed: 15264254]

63. Hanwell MD, Curtis DE, Lonie DC, Vandermeersch T, Zurek E, and Hutchison GR (2012). Avogadro: an advanced semantic chemical editor, visualization, and analysis platform. J. Cheminf. 4, 17. 10.1186/1758-2946-4-17.

64. Frisch MJ, Trucks GW, Schlegel HB, Scuseria GE, Robb MA, Cheeseman JR, Scalmani G, Barone V, Mennucci B, Petersson GA, et al. (2013). Gaussian 09, Revision D.01 (Gaussian, Inc.).

65. Scott DJ, Gunn NJ, Yong KJ, Wimmer VC, Veldhuis NA, Challis LM, Haidar M, Petrou S, Bathgate RAD, and Griffin MDW (2018). A novel ultra-stable, monomeric green fluorescent protein for direct volumetric imaging of whole organs using CLARITY. Sci. Rep. 8, 667. 10.1038/s41598-017-18045-y. [PubMed: 29330459]

66. Sarkar CA, Dodevski I, Kenig M, Dudli S, Mohr A, Hermans E, and Plückthun A (2008). Directed evolution of a G protein-coupled receptor for expression, stability, and binding selectivity. Proc. Natl. Acad. Sci. USA 105, 14808–14813. 10.1073/pnas.0803103105. [PubMed: 18812512]

67. Zhao H, and Zha W (2006). In vitro ‘sexual’ evolution through the PCR-based staggered extension process (StEP). Nat. Protoc. 1, 1865–1871. 10.1038/nprot.2006.309. [PubMed: 17487170]

68. Schaffner W, and Weissmann C (1973). A rapid, sensitive, and specific method for the determination of protein in dilute solution. Anal. Biochem. 56, 502–514. 10.1016/0003-2697(73)90217-0. [PubMed: 4128882]

69. Schanda P, and Brutscher B (2005). Very fast two-dimensional NMR spectroscopy for real-time investigation of dynamic events in proteins on the time scale of seconds. J. Am. Chem. Soc. 127, 8014–8015. 10.1021/ja051306e. [PubMed: 15926816]

70. Kupce E, and Freeman R (1993). Polychromatic selective pulses. J. Magn. Reson. 102, 122–126. 10.1006/jmra.1993.1079.

71. Kupce E, Boyd J, and Campbell ID (1995). Short selective pulses for biochemical applications. J. Magn. Reson. B 106, 300–303. 10.1006/jmrb.1995.1049. [PubMed: 7719630]

72. Kazimierczuk K, and Orekhov VY (2011). Accelerated NMR spectroscopy by using compressed sensing. Angew. Chem., Int. Ed. Engl. 50, 5556–5559. 10.1002/anie.201100370. [PubMed: 21538743]

Highlights

- Methionine residues sense concerted GPCR motions on the sub-μs timescale
- GPCR ensembles contain multiple meta-states including the crystalized conformer
- The degree of global dynamics correlates with ligand pharmacological efficacy

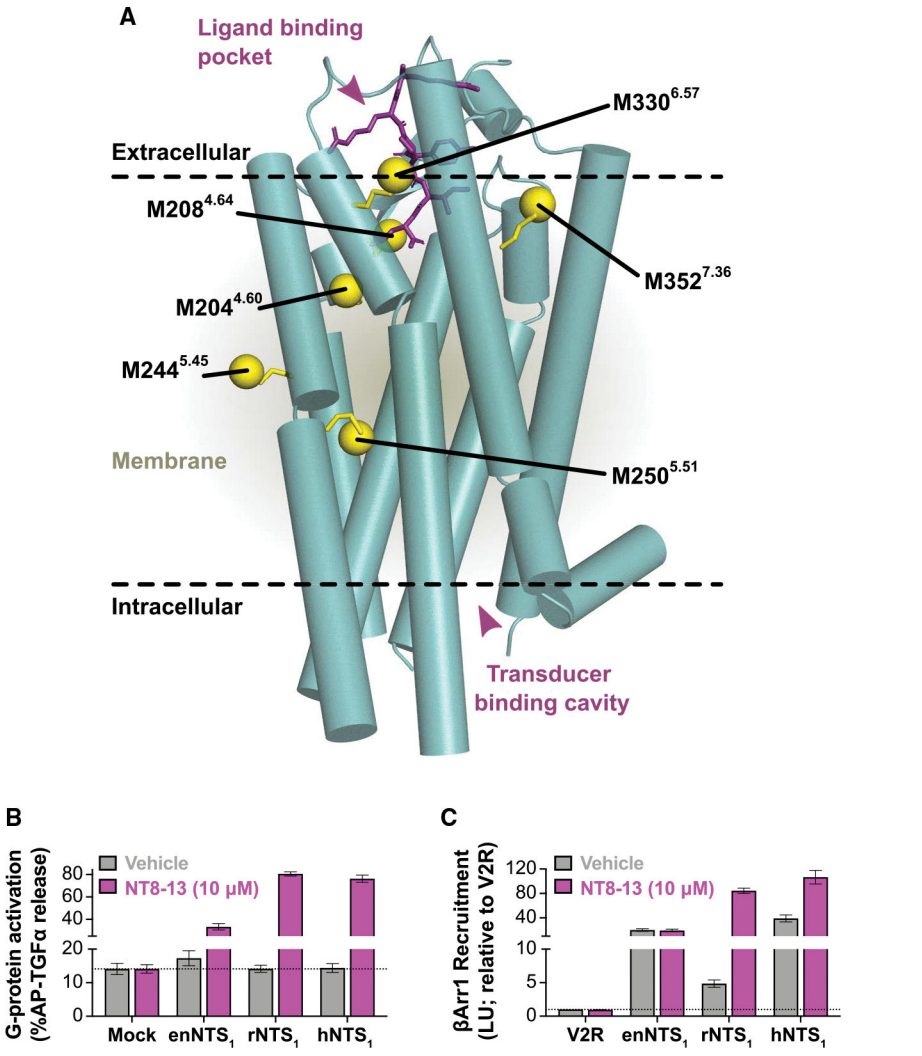

Figure 1. Ligand-induced chemical shift changes observed for $^{13}CH_3$-methionine-labeled enNTS$_1$ΔM4

(A) Cylindrical representation of thermostabilized rNTS$_1$ (PDB: 4BWB) with labeled methionine methyl groups shown as yellow spheres (superscript is Ballesteros-Weinstein nomenclature[25]) and NT8-13 shown as purple sticks.

(B) NT8-13 promotes enNTS$_1$ΔM4-mediated G protein activation in a TGF-α shedding assay using HEK293A cells.[27] Cells were transfected with mock, enNTS$_1$ΔM4, rat NTS$_1$ (rNTS$_1$), or human NTS1 (hNTS$_1$) then stimulated with vehicle or 10 μM NT8-13 (magenta). Error bars represent SEM from three independent experiments that each included at least three replicates per ligand concentration.

(C) βArr1 recruitment was measured by a NanoBiT-based assay using HEK293A cells.[28] Cells were transfected with V2R, enNTS$_1$ΔM4, rNTS$_1$, or hNTS$_1$ and then stimulated with vehicle or 10 μM NT8-13 (magenta). Error bars represent SEM from three independent experiments that each included at least three replicates per ligand concentration.

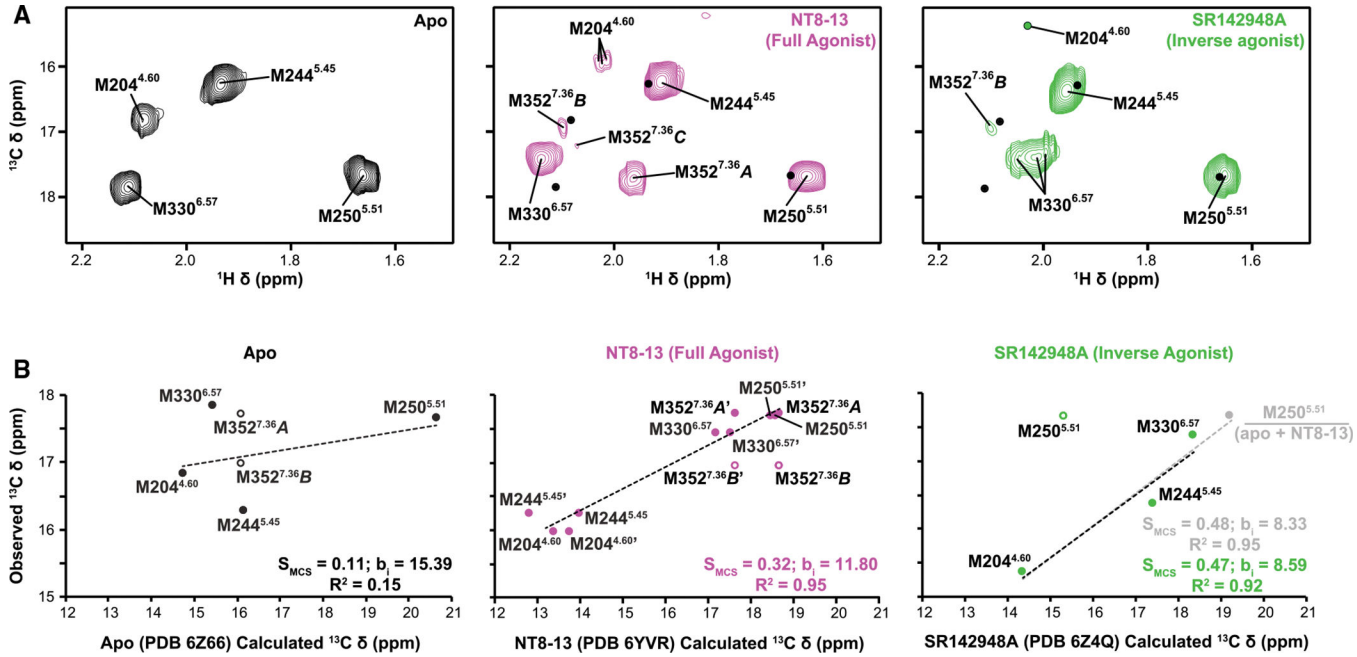

Figure 2. Ligand-induced chemical shift changes observed for $^{13}CH_3$-methionine labeled enNTS$_1$ΔM4

(A) ^{1}H-^{13}C HMQC spectra of [$^{13}C^{\varepsilon}H_3$-methionine]-enNTS$_1$ΔM4 in the absence and presence of orthosteric ligands. All spectra were recorded at 600 MHz with protein concentrations of 66 μM. Each displayed spectrum represents a single experiment.

(B) Linear correlation between DFT-calculated and experimental ^{13}C chemical shift values. There are no error estimates for the calculated chemical shifts because repeating DFT calculations would yield identical results. Error bars for the experimental chemical shifts represent the standard deviation, calculated for each individual methionine residue, from two independently prepared NT8-13:[$^{13}C^{\varepsilon}H_3$-methionine]-enNTS$_1$ΔM4 samples. In all cases, the size of the error bar is smaller than the symbol. All observable resonances are included in the scatterplots, but only filled circles are fitted to linear regressions. In spectra where a single methionine is assigned to multiple observable resonances, only the most populated (i.e., highest intensity) peak is fitted; the lower intensity peak is almost always an outlier (open circle). Linear regression of the DFT-calculated and observed ^{13}C chemical shifts are generally well correlated ($0.86 \leq R^2 \leq 0.95$) apart from the apo state ($R^2 = 0.15$). The slope of the line (S_{MCS}) can be interpreted as global side-chain order with values ranging from one (rigid) to zero (completely averaged). The magnitude of the line's y intercept (b_i) also reflects the protein's overall flexibility. For the NT8-13 state, the experimental chemical shifts were simultaneously fitted to calculated chemical shifts from both chain A (indicated without a prime) and chain B (indicated with a prime) of the X-ray structure. Fitting the calculated chemical shifts of chain A and chain B individually resulted in S_{MCS} of 0.33 (R^2 = 0.99; b_i = 11.61) and 0.32 (R^2 = 0.92; b_i = 11.87), respectively. Because the M250$^{5.51}$ side chain in the SR142948A crystal structure (PDB: 6Z4Q) was orientated drastically different from all other published crystal structures, we fitted the linear regression two ways: (1; black line) excluding M250$^{5.51}$ and (2; gray line) including the average of DFT-calculated chemical shifts for M250$^{5.51}$ from apo and NT8-13-bound crystal structures.

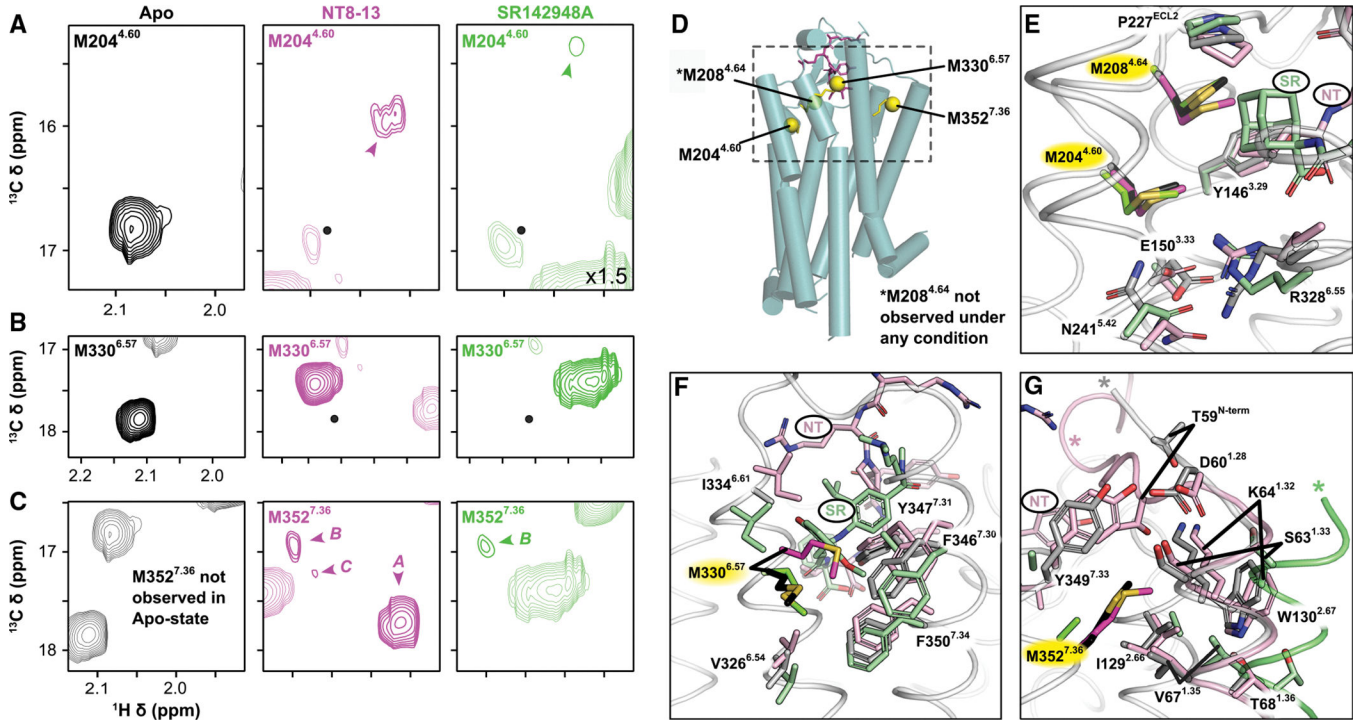

Figure 3. Ligand-dependent chemical shift perturbations in extracellular methionine residues

(A–C) Extracted ^{1}H-^{13}C HMQC spectral regions of M204$^{4.60}$ (A), M330$^{6.57}$ (B), and M352$^{7.36}$.(C) for apo (black), NT8-13 agonist-bound (magenta), and SR142948A inverse agonist-bound (green) enNTS$_1$ΔM4; black dots in ligand-bound spectra denote the respective residue's position in the apo state. The resonances of other residues within the extracted region are drawn at 50% transparency. All spectra were recorded at 600 MHz with protein concentrations of 66 μM. Each displayed spectrum represents a single experiment.

(D) Positions of extracellular methionine residues in thermostabilized rNTS$_1$ (PDB: 4BWB); M204$^{4.60}$ resides within the orthosteric ligand-binding site, M330$^{6.57}$ at the extracellular tip of TM6 facing TM5, and M352$^{7.36}$ at the extracellular tip of TM7 facing TM1. M208$^{4.46}$ was not observed.

(E–G) Local environments of methionine residues observed in crystal structures of apo (methionine, black, and surrounding residues, gray; PDB: 6Z66), NT8-13-bound (methionine, magenta, and surrounding residues, light pink; PDB: 6YVR), and SR142948A-bound (methionine, green, and surrounding residues, pale green; PDB: 6Z4Q) NTS$_1$-H4.[23] Portions of the ligands are labeled NT (NT8-13) and SR (SR142948A). In (E) and (F), the backbone trace is only shown for the apo state (light gray). In (G), cartoons of TM1 and the N terminus are illustrated for all structures. See Figure S8 for more detail.

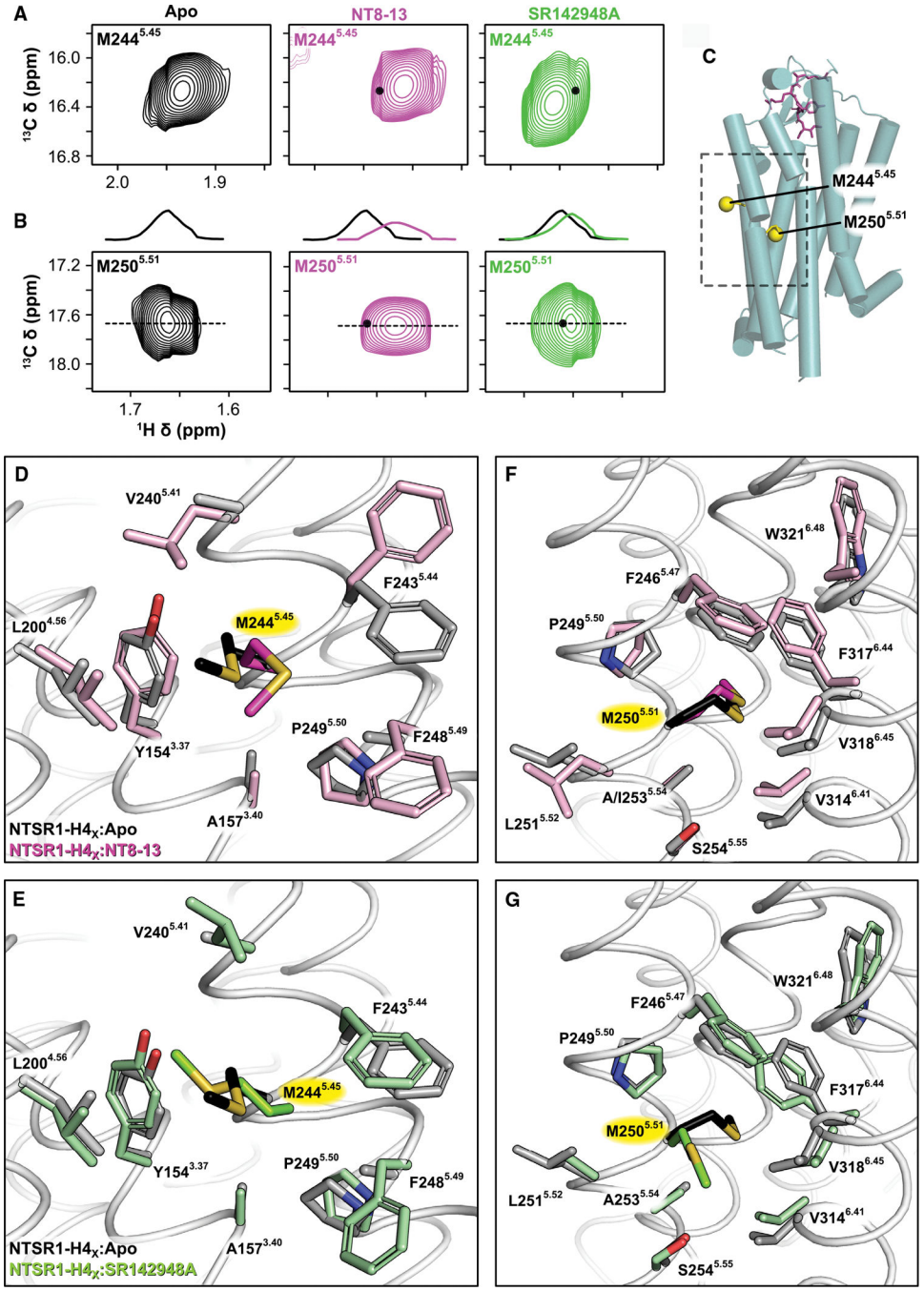

Figure 4. Ligand-dependent chemical shift perturbations for transmembrane domain methionine residues

(A and B) Extracted ^{1}H-^{13}C HMQC spectral regions of M244$^{5.45}$ (A) and M250$^{5.51}$ (B) for apo (black), NT8-13 agonist-bound (magenta), and SR142948A inverse agonist-bound (green) enNTS$_1$ΔM4; black dots in ligand-bound spectra denote the respective residue's position in the apo state. All spectra were recorded at 600 MHz with protein concentrations of 66 μM. Each displayed spectrum represents a single experiment.

(C) Positions of transmembrane methionine residues in thermostabilized rNTS$_1$ (PDB: 4BWB); M244$^{5.45}$ resides approximately one turn prior to the highly conserved P249$^{5.50}$

and faces TM4, while M250$^{5.51}$ is located immediately after P249$^{5.50}$ and points directly into the PIF motif.

(D–G) Local environments of transmembrane methionine residues observed in crystal structures. Apo-state $NTSR_1$-$H4_X$ (methionine, black, and surrounding residues, gray; PDB: 6Z66[23]). Only the backbone trace is shown for the apo state (gray cartoon). See Figure S9 for more detail.

(D and F) NT8-13 agonist-bound structure of $NTSR_1$-$H4_X$ (methionine, magenta, and surrounding residues, light pink; PDB: 6YVR[23]).

(E and G) SR142948A inverse agonist-bound structure of $NTSR_1$-$H4_X$ (methionine, green, and surrounding residues, pale green; PDB: 6Z4Q[23]).

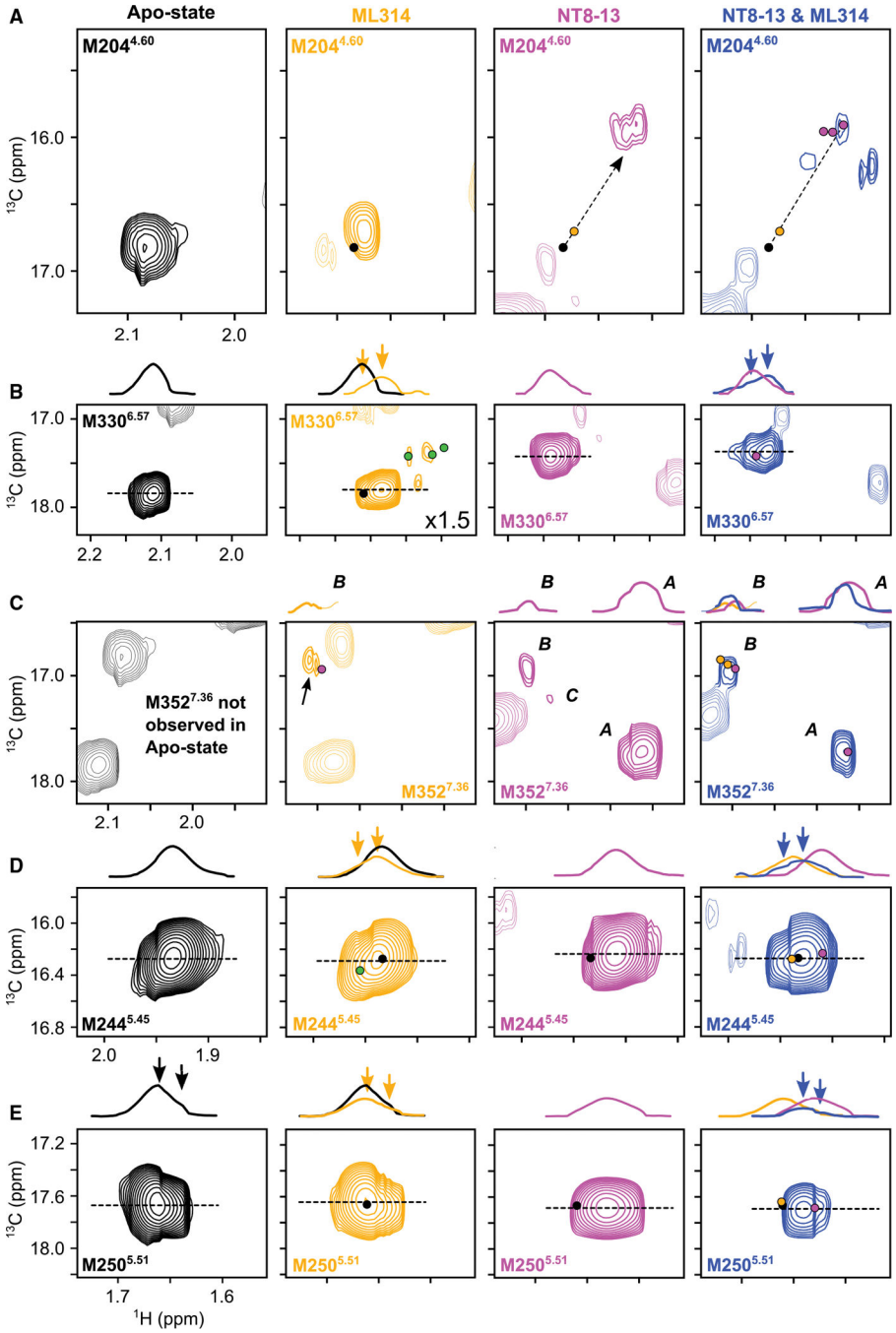

Figure 5. Methionine resonance perturbations near the connector region are suggestive of functional selectivity

(A–E) Extracted spectral regions of individual methionine residues for apo (black), M314 ago-BAM-bound (orange), NT8-13 agonist-bound (magenta), and ML314 and NT8-13 bound (blue) enNTS$_1$ΔM4. The dots in ligand-bound spectra denote the respective residue's position in the presence of alternative ligands (e.g., an orange dot marks the respective residue's position in the ML314-bound spectrum). Resonances also observed in SR142948A inverse agonist-bound spectra are marked with green dots. All spectra were recorded at 600

MHz with protein concentrations of 66 μM. Each displayed spectrum represents a single experiment.

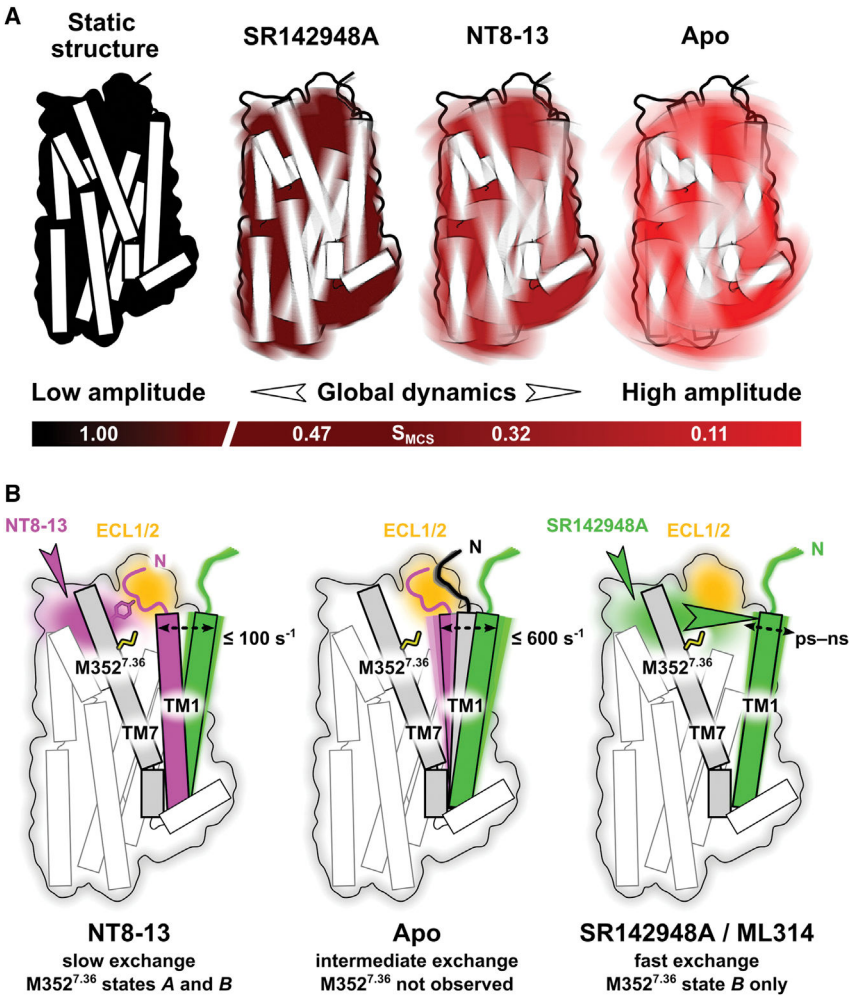

Figure 6. Illustration of ligand-mediated global and local GPCR dynamics

(A) DFT calculations suggest that ligands differentially effect the amplitude of concerted enNTS$_1$ motions as represented by the S_{MCS} global order parameter.

(B) The high linear correlation between DFT-calculated and experimentally observed chemical shifts lends confidence to spectral interpretation based upon the “rigid-limit” crystallographic structures.

KEY RESOURCES TABLE

REAGENT or RESOURCE	SOURCE	IDENTIFIER
Antibodies		
Anti-FLAG-epitope tag monoclonal antibody (Clone 1E6)	FujiFilm Wako Pure Chemicals	Cat# 014-22383; RRID: AB_10659717
Goat anti-mouse IgG secondary antibody conjugated with Alexa Fluor 488	Thermo Fisher Scientific	Cat# A-11001; RRID: AB_2536161
Bacterial and virus strains		
Escherichia Coli DH5α	Thermo Fisher Scientific	Cat# 18265017
Escherichia Coli OverExpress C43(DE3)	Sigma-Aldrich	Cat# CMC0019
Chemicals, peptides, and recombinant proteins		
PrimeSTAR HS DNA polymerase	Takara	Cat# R010B
Phusion HF DNA polymerase	NEB	Cat# M0530S
Bioline Isolate II kit	Bioline	Cat# BIO-52067
Restriction Endonuclease BamHI-HF	NEB	Cat# R3136S
Restriction Endonuclease NheI-HF	NEB	Cat# R3131S
Agonist peptide NT8-13 (StEP, Assignment NMR)	Purar chemicals	N/A
Agonist peptide NT8-13 (enNTS$_1$ΔM4 &enNTS$_1$ΔM4_M330L NMR, functional assays)	Dr Piotr Mroz, Indiana University	N/A
Fluorescent peptide FAM-NT8-13	GL Biochem	Cat# 462157
Fluorescent peptide 5-TAMRA-NT8-13	GL Biochem	Cat# 516054
Inverse agonist SR142948A	Axon MedChem	Cat# Axon 1255
Dimethyl sulfoxide-d6 (DMSO-d6)	Sigma-Aldrich	Cat# 151874
Oxoid tryptone	Thermo Fisher Scientific	Cat# LP0042
Oxoid yeast extract	Thermo Fisher Scientific	Cat# LP0021
NaCl	Sigma-Aldrich	Cat# S9888
KCl	Sigma-Aldrich	Cat# P3911
$MgCl_2 \cdot 6H_2O$	Sigma-Aldrich	Cat# M2670
Ampicillin	Goldbio	Cat# A-301
Sucrose	Sigma-Aldrich	Cat# S0389
Glucose	Sigma-Aldrich	Cat# G5767
Isopropyl β-D-1-thiogalactopyranoside (IPTG)	Goldbio	Cat# I2481C
Tris HCl	Thermo Fisher Scientific	Cat#15506017
HEPES	Sigma-Aldrich	Cat# H3375
Na_2SO_4	Sigma-Aldrich	Cat# 239313
KH_2PO_4	Sigma-Aldrich	Cat# P0662
K_2HPO_4	Sigma-Aldrich	Cat# P3786
Na_2HPO_4	Sigma-Aldrich	Cat# S9763
NH_4Cl	Sigma-Aldrich	Cat# 213330
NaOH	Sigma-Aldrich	Cat# 221465

REAGENT or RESOURCE	SOURCE	IDENTIFIER
$MgSO_4$	Sigma-Aldrich	Cat# 230391
Trace elements solution	Prepared according to Cai et al.[59]	N/A
Thiamine	Sigma-Aldrich	Cat# T1270
$^{13}CH_3$-Methionine	Cambridge Stable Isotopes	Cat# CLM-206
Lysine	Sigma-Aldrich	Cat# L5626
Threonine	Sigma-Aldrich	Cat# T8625
Phenylalanine	Sigma-Aldrich	Cat# P2126
Leucine	Sigma-Aldrich	Cat# L8000
Isoleucine	Sigma-Aldrich	Cat# I2752
Valine	Sigma-Aldrich	Cat# V0500
D_2O (99.9%)	Cambridge Stable Isotopes	Cat# DLM-4-1
Sodium 2,2-dimethyl-2-silapentane-5-sulfonate (DSS)	Cambridge Stable Isotopes	Cat# DLM-32
NaN3	Sigma-Aldrich	Cat# S2002
Roche cOmplete EDTA-free protease inhibitor tablets	Sigma-Aldrich	Cat# 5056489001
Phenylmethylsulfonyl fluoride (PMSF)	Sigma-Aldrich	Cat# 78830
Detergent n-decyl-β-D-maltopyranoside (DM)	Anatrace	Cat# D322S
Detergent n-dodecyl-β-D-maltopyranoside (DDM)	Anatrace	Cat# D310
d_{25}-DDM	FB Reagents	N/A
Cholesterol hemi-succinate (CHS)	Avanti Polar Lipids	Cat# 850524
3-[(3-Cholamidopropyl)dimethylammonio]-1-propanesulfonate hydrate (CHAPS)	Sigma-Aldrich	Cat# C3023
Talon Cobalt resin	Takara	Cat# 635504
Imidazole	Sigma-Aldrich	Cat# I2399
HRV 3C-protease	Produced in-house	N/A
DMEM	Nissui Pharmaceutical	Cat# 05919
FBS (Gibco)	Sigma-Aldrich	Cat# 173012
Glutamine	Thermo Fisher Scientific	Cat# 21051024
Penicillin G	Sigma-Aldrich	Cat# P3032
Streptomycin	Thermo Fisher Scientific	Cat# 11860-038
Polyethylenimine Max solution	Polysciences	Cat# 24765-1
Trypsin	Thermo Fisher Scientific	Cat# 27250-018
P-nitrophenylphosphate (p-NPP)	FUJIFILM Wako Pure Chemical	Cat# 145-02344
Opti-MEM	Thermo Fisher Scientific	Cat# 31985-070
Coelenterazine	Carbosynth	Cat# EC14031
Goat serum	Nippon Bio-test Laboratories	Cat# 0208-01
Deposited data		
[$^{13}C^{\varepsilon}H_3$-methionine]-enNTS$_1$ chemical shifts in apo state	Biological Magnetic Resonance Data Bank (BMRB)	BMRB: 51728
[$^{13}C^{\varepsilon}H_3$-methionine]-enNTS$_1$ chemical shifts in NT8-13 bound state	Biological Magnetic Resonance Data Bank (BMRB)	BMRB: 51735
[$^{13}C^{\varepsilon}H_3$-methionine]-enNTS$_1$ chemical shifts in SR142948A bound state	Biological Magnetic Resonance Data Bank (BMRB)	BMRB: 51736

REAGENT or RESOURCE	SOURCE	IDENTIFIER
[$^{13}C^{e}H_3$-methionine]-enNTS$_1$ chemical shifts in ML314 bound state	Biological Magnetic Resonance Data Bank (BMRB)	BMRB: 51737
[$^{13}C^{e}H_3$-methionine]-enNTS$_1$ chemical shifts in NT8-13 and ML314 bound state	Biological Magnetic Resonance Data Bank (BMRB)	BMRB: 51738
Experimental models: Cell lines		
HEK293A cells	Thermo Fisher Scientific	Cat# R70507
Oligonucleotides		
rNTS1B5-BamFwd: CATCATGGATCCACCTC TGAATCTGACACCGC	Sigma-Aldrich	N/A
rNTSI-NheRev: CATCATGCTAGCGGTAGAGA ACGCGTGGTTAG	Sigma-Aldrich	N/A
Recombinant DNA		
Plasmid pDS170-enNTS$_1$	Bumbak et al.[24]	N/A
Plasmid pDS11-SacB	Genscript	N/A
Plasmid pDS170-SacB	Genscript	N/A
Plasmid pCAGGS-ssHA-FLAG-rNTS$_1$	This study	N/A
Plasmid pCAGGS-ssHA-FLAG-hNTS$_1$	This study	N/A
Plasmid pCAGGS-ssHA-FLAG-enNTS$_1$	This study	N/A
Plasmid pCAGGS-ssHA-FLAG-enNTS$_1$ΔM4	This study	N/A
Plasmid pCAGGS-AP-TGF-α	Inoueetal., 2019[29] (PMID 31160049)	N/A
Plasmid pCAGGS-ssHA-FLAG-rNTS$_1$-SmBiT	This study	N/A
Plasmid pCAGGS-ssHA-FLAG-hNTS$_1$-SmBiT	This study	N/A
Plasmid pCAGGS-ssHA-FLAG-enNTS$_1$-SmBiT	This study	N/A
Plasmid pCAGGS-ssHA-FLAG-enNTS$_1$ΔM4-SmBiT	This study	N/A
Plasmid pCAGGS-LgBiT-βArr1	Shihoya et al.[28] (PMID 30413709)	N/A
Gene enNTS$_1$ΔM10	Genscript	N/A
Gene enNTS$_1$ΔM7	Genscript	N/A
Gene enNTS$_1$ΔM6	Genscript	N/A
Gene enNTS$_1$ΔM5	Genscript	N/A
Gene enNTS$_1$ΔM4	Genscript	N/A
Gene enNTS$_1$ΔM4_M330L	Genscript	N/A
Software and algorithms		
Topspin 3.6	Bruker Corporation	http://www.bruker.com/en/products-and-solutions/mr/nmr-software/topspin.html
qMDD 3.2	Kazmierczuk et al.[60]	http://mddnmr.spektrino.com
NMRPipe	Delaglio et al.[61]	http://www.ibbr.umd.edu/nmrpipe

REAGENT or RESOURCE	SOURCE	IDENTIFIER
NMRFAM-Sparky 3.131	Goddard, T.D. and Kneller, D.G., University of California, San Francisco	http://nmrfam.wisc.edu/nmrfam-sparky-distribution/
Chimera 1.12	Pettersen et al.[62]	http://www.cgl.ucsf.edu/chimera
Avogadro 1.2.0	Hanwell et al.[63]	http://www.avogadro.cc
Gaussian 09	Frisch et al.[64]	http://www.gaussian.com
Prism 8	GraphPad Software	http://www.graphpad.com/scientific-software/prism
PyMol 2.4.0	Schroedinger Inc.	http://pymol.org/2/#opensource
Other		
Electroporator Eppendorf Eporator	Eppendorf	Cat# 4309000035
Electroporation cuvettes Biorad GenePulser 0.2cm gap	Biorad	Cat# 1652082
Fluorescence activated cell sorter FACSAria III	BD Biosciences	N/A
Flow cytometer LSR Fortessa X-20 FACS	BD Biosciences	N/A
Concentrator Amicon 30 kDa MWCO	Merck-Millipore	Cat# UFC903024
Cation exchange chromatography column 5 mL HiTrap SP HP	Cytiva Lifesciences	Cat# 17115201
Nickel affinity chromatography column 1 mL Ni-NTA HisTrap	Cytiva Lifesciences	Cat# 17524701
Size exclusion chromatography column Superdex S200 Increase 10/300 GL	Cytiva Lifesciences	Cat# 28990944
Purification system Akta Pure 25-M	Cytiva Lifesciences	Cat# 29018226
Spectrometer 800MHz Bruker Avance II	Bruker Corporation	N/A
Spectrometer 600MHz Bruker Avance III Neo	Bruker Corporation	N/A
Spectrometer 800MHz Varian	Varian Corporation	N/A
NMR tubes 5mm Shigemi BMS-005B	Sigma-Aldrich	Cat# Z543349
NMR tubes Willmad 3mm thin wall precision	SP Willmad-LabGlass	Cat# 335-PP-8
Cellstar 6-well culture plates	Greiner Bio-One	Cat# 657160
White 96-well microplates	Greiner Bio-One	Cat# 655904
Black 96-well V-bottom microplates	Greiner Bio-One	Cat# 651209
Microplate reader SpectraMax 340 PC384	Molecular Devices	N/A
Microplate reader SpectraMax L, 2PMT	Molecular Devices	N/A